Utrecht University

Impervious surface mapping using satellite data and runoff modelling in Amersfoort, NL

Written by:
Yuannan Wang

Supervised by:
PROF. DR. S. M. DE JONG & DR. M. J. Zeylmans van EMMICHOVEN

Utrecht University
Geohazards and Earth Observation, Earth Surface and Water, Geoscience.

Universiteit Utrecht

Abstract

An increase of urban flash flood issues has been observed throughout the world in recent years. It has led to enormous losses and people were killed. The increase of urban flash flooding is mainly due to more intensive rain events and more ground surfaces converted into impervious surfaces. Although the runoff mechanism and process have been widely studied, the runoff modeling on the basis of impervious surface mapping is still a new aspect to the study of urban flooding.

The main objective of this study is to evaluate various approaches for impervious surface mapping on the basis of satellite images, and evaluating the hydrological impact of impervious surface expansion in Amersfoort by a runoff model. The study area is located at Amersfoort, which is the second largest city in Utrecht Province in the Netherlands. A fast urbanization process took place over the last 30 years. In addition, Amersfoort is a high risk area of urban (flash) flooding because it is located next to an elevated hill in the south-west.

The regression modeling method and the Normalized Linear Spectral Mixing Analysis (NLSMA) methods were applied to Landsat images. Accuracy assessment of these two methods showed that impervious areas mapped by NLSMA had a higher accuracy. The Decision Tree Classification (DTC) method was applied to FORMOSAT-2 image. An overall accuracy of 92% was achieved by the error matrix. Uncertainties, advantages and constraints for these three methods were compared and discussed.

The runoff responses were evaluated by linking the impervious surfaces maps to a straightforward rainfall-runoff model. A number of one-hour rainfall events with various intensities were worked out and the results showed that the Amersfoort railway station is the most vulnerable place o runoff in case of an intensive rainfall event. The investigated area can bear a one-hour rainfall with a return time of less than two years. Risk maps of buildings for every scenario were worked out. Risk maps are very important for city managers as they can guide them to distribute the limited relief resources efficiently.

Keywords: Impervious surface mapping, multi-temporal remote sensing, runoff analysis, Amersfoort

Acknowledgements

I would like to take this opportunity to thank all the people that provide their knowledge, share their experience and spend their time to help me complete my master thesis.

First, I would like to thank you Steven de Jong. Your office door is always open to me and I really appreciate for you spending your valuable time meeting with me. Every meeting I spent with you is an improvement for my thesis. Thank you for the book and paper you provided me, these literatures gave me a clear clue to conduct my study.

A big thank you is given to Maarten J. Zeylmans van Emmichoven for his ultimate support and instructions on my hands-on applications on remote sensing and GIS. I would also like to thank you for authorizing me to download satellite data that I used for analysis. That gave me a very quick and clear start at the beginning of this study.

Cheers to my family and friends for all the companionship and help throughout the long process of my thesis study. Cheers to myself for all the hard working finally deserves!

Content

List of Figures, Tables and Flowcharts

Chapter 2

Chapter 3

Chapter 4

Chapter 5

Chapter 6

(C): Spatial runoff patterns for a rainfall event of 18 mm/hour; (D): Spatial runoff patterns for a rainfall event of 23 mm/hour.

Figure 34 The risk map for buildings in a case of 23 mm/hour storm.

Chapter 7

Figure 36 Bare soil classified as an impervious surface. IPO Luchtfoto actueel (2011) is on the left and the impervious surface percentage map is on the right.

Figure 37 An example of the shade effect in residential area. The impervious surface fraction calculated by NLSMA (left rectangle) is only 55%, while the actual fraction is measured as high as 70% (right rectangle).

Figure 38 Underestimation in impervious surface areas due to the shade effect.

Figure 39 Comparisons between impervious areas map with a different threshold to separate soil and impervious surfaces. (A): Soil threshold-1.0; (B): Soil threshold-2.0;

Table 15 A detail comparison between NLSMA and regression modeling. Less developed areas: <50% imp; Developed areas: >50% imp.

Figure 40 Runoff process in model and in reality. (A): Runoff process in the model; (B): Real runoff process.

1. Introduction

1.1 Urbanization and impervious surface increase

With an increasing number of people moving to cities, the urban area expands to accommodate them. In recent years, rapid urbanization processes have become a global trend. In Asia, several large cities such as Dhaka, Mumbai, Seoul and Beijing are home to over 20 million people. In addition, several economic development zones such as the Perl River Delta region, Shanghai-Suzhou region and Hong Kong-Shenzhen-Guangzhou mega-region in China are forecasted to exceed 40 million people within the coming decade. Outside Asia, several large cities such as New York, Mexico City, Paris is hosting over 20 million people and this number is still boosting all along (Henderson, 2003).

As the urbanization process continues, several environmental issues have been recognized in recent years. From a perspective of sociology, fast urbanization leads to several problems such as tight energy supply, traffic congestion, increased crimes and so on. On the other hand, some phenomenon such as urban flash flooding and heat island effects have become a threat to all the citizens living in the cities. Apart from the increased frequency of extreme weather events, an important reason behind these environmental issues is the quick process of turning previous surfaces into impervious surfaces during the urbanization (Weng, 2012).

Impervious surfaces are referred to as the anthropogenic features through which water cannot infiltrate into the soil, such as roads, driveways, parking lots, houses, buildings and so on. Creating impervious surfaces on the natural land leads to that less water can infiltrate into ground. Therefore, converting pervious surfaces into impervious surfaces at a large scale may lead to a significant runoff process in case of intensive rainfall. This runoff process is more significant in areas with topography due to the generated runoff and water concentration on steep slopes (Boegh *et al.*, 2009). Furthermore, large volumes of runoff flows may lead to flash flooding in a watershed or in the urban area located downstream, creating a potential damage to the infrastructures and buildings in the cities. In addition, with less water infiltrating into the ground in the long term, the water cycling process in a watershed may be slowed down and the water quality and water availability will reduced dramatically (Amir & Ronald, 2004).

A prerequisite for the quantitative study of environmental issues caused by the increasing impervious surface is to obtain detailed information of impervious surface in an urban area. Knowledge on impervious surfaces, especially the magnitude, location, geometry, spatial patterns and the perviousness-imperviousness ratio, is significant to a range of issues and themes in environmental science (Weng, 2012). Therefore, accurate impervious surface mapping in the urban areas has recently attracted unprecedented attention from natural scientists throughout the world (Weng, 2012).

1.2 Objectives and structure overview

This thesis aims at performing and evaluating various approaches for impervious surface mapping on the basis of satellite images, and evaluating the runoff responses of the impervious surface expansion in Amersfoort by a model simulation. As the satellite data is more appropriate than the aerial photographs for mapping impervious surface areas at a large scale such as a city, therefore the satellite data were used in this study. In addition, considering that the satellite images are available even reaching back to 30 years before the present, the change of impervious surface areas in Amersfoort can be well delineated by satellite data. Several research questions and sub-questions were proposed according to the thesis objectives.

- **How can impervious areas in cities are mapped by remote sensing at what accuracy.**
    - What methods are available? How to select an appropriate method?
    - How to extract impervious surface from satellite images?
    - What is the obtained mapping accuracy?
    - What are the advantages and constrains for different approaches?
- **How has the impervious surface areas in Amersfoort expanded in the last 30 years?**
    - What were the spatial patterns of impervious areas in the past and how the spatial patterns changes?
- **What is the increase of runoff and what is the risk level of infrastructure and buildings for an urban flood in a case of intensive rainfall?**
    - What is the simulated spatial pattern of runoff?
    - Is it possible to reduce flood risk in Amersfoort?

The structure of the thesis is described in the following. The theoretical background for impervious surface mapping and runoff analysis is described in Chapter 2. Chapter 3 describes the study area and Chapter 4 presented the satellite data used for this study. Chapter 5 explains the applied methods and procedures for impervious surface mapping with medium and high spatial resolution images. Moreover, the runoff model is described and runoff analysis scheme is explained. Chapter 6 presents the results of impervious surface mapping and runoff modeling. Discussions about the errors associated with various mapping methods and runoff analysis are provided in Chapter 7. In Chapter 8, conclusions regarding the research questions are given. Future research is present in Chapter 9.

2. Theoretical background

The Theoretical background for impervious areas mapping and runoff modeling is described in the following.

2.1 Differences in dealing with Medium and High spatial resolution images.

The approaches used for impervious surface mapping with respective to medium and high spatial resolution are different. The medium spatial resolution image is referred to as an image with a pixel size of more than 30 meters, while the high spatial resolution image has a pixel of less than 10 meters.

Due to the coarse pixel in medium resolution images, the mixed pixel effect cannot be ignored. Figure 1 shows the mixed pixel effect for a Landsat image. Within one pixel (outlined in red), several land covers such as paved road, grass and cement court are present. If applying the pixel-based classification to this image, this pixel will be classified as vegetation due to grass is dominant. Thus impervious surface areas within this pixel are completely lost. Therefore, simple pixel-based classification will lead to un-accurate result to a large extent. Instead, other than simple pixel-based classifications, estimating the proportion of impervious surface within one pixel is the way to map the impervious areas for images with mixed pixel effect.

On the other hand, the mixed pixel effect is very small when dealing with high spatial resolution images because the fine-pixel image can delineate the urban landscape in a great detail. Therefore, some specific pixel-based classification can be directly employed to map the impervious areas in cities for high spatial resolution images.

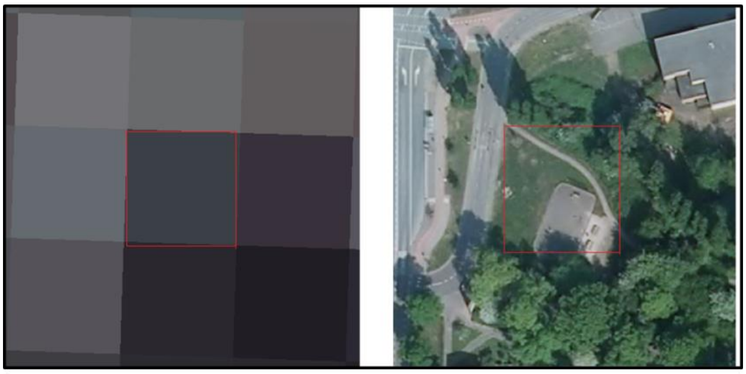

Figure 1 Mixed pixel effect of Landsat image on the left compared to IPO Luchtfoto actueel (2011) on the right.

2.2 V-I-S model

The theoretical foundation of impervious areas mapping with respective to medium resolution images is the V-I-S model proposed by Ridd (1995). Ridd assumed that the complex urban landscapes can simply be delineated as a mixture of vegetation, impervious surfaces and soil (V-I-S model). In the urban area, impervious areas, vegetation and soil have their own distributed features. To be specific, impervious surface is spatially concentrated, consisting of a CBD (Central Business District), high- or low- density residential and commercial areas. The vegetation component mainly contains grass and trees and they are mostly distributed in the suburban area or along channels or rivers. As for the soil, it may exist within and outside of the urban area and is a major source of pervious surface. A number of studies on urban applications based on V-I-S model have been explored. Rashed et al. (2001) described the urban composition of Cairo, Egypt as vegetation, impervious surface, soil, and shade, and consequentially applied the derived urban composition into detailed land use classification; Lu and Weng (2004) employed four components (green vegetation, impervious surface, soil and shade) to describe urban/rural environments. These studies have proven that the V–I–S model based approach has potential to describe land covers and land uses in urban applications. Therefore, the V-I-S model will be used in this study to map the impervious areas in an urban area.

2.2 Runoff process

The foundation of the runoff model, to which the impervious surface map will be linked, is explained in the following.

Figure 2 shows a general overview of the water balance in a case of rainfall. Runoff results directly from rain and an exceedance of the infiltration capacity. Before the rainfall hit the ground, a small amount is intercepted by trees. When the rainfall falls on the ground, it will start to infiltrate into the ground. After the ground is saturated, the rainfall will remain on the ground surface and flow to the lower places if the local terrain is elevated. At the same time, a very small amount of water will be evaporated. Considering that the evaporation is a very slow process, so that the amount of evaporation is not included into the runoff modeling. Therefore, precipitation, infiltration capacity and elevated ground surface can be concluded as three key factors in the runoff simulations.

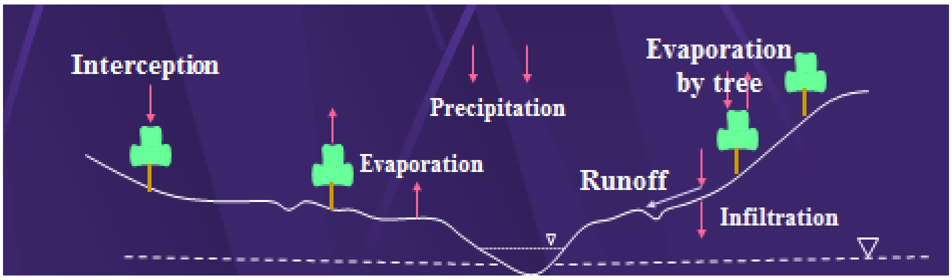

Figure 2 Water balance in a case of rainfall

Source: Bing Ruifang, (2004). Principle of Hydrology. China WaterPower Press. pp: 254.

Infiltration capacities vary between different land covers. The forest area and bare soil normally have a relative high infiltration capacity while most of the man–made objectives (such as paved roads, buildings, parking lots) are almost totally impervious. Therefore, runoff will mainly occur on the impervious areas. In addition, a hilly area will accelerate the runoff process because the small runoffs can converge together, resulting in a large volume of runoff flow flowing to downstream.

Since variations in land cover and the impervious areas play a key role in the generation of runoff and possible flooding downstream. Remote sensing images are suitable tools for assessing impervious areas and flood risk mapping.

3. Study area

The study area is located at Amersfoort city in Netherlands.

Amersfoort (52°9’N, 5°23’E) is located in the central part of Netherlands. It is a municipality and the second largest city in the province of Utrecht. In the history, several significant expansions of Amersfoort were well documented. The first enlargement of Amersfoort was around 1400 after it was granted city rights in 1259. In 18th century, the city expanded again because of the cultivation of tobacco and the first establishment of a railway to Amersfoort (Figure 3-(A)). 70,000 inhabitants lived in Amersfoort during 1970s whilst currently the residents have boosted to over 150,000. With the great in-movement of citizens, Amersfoort started to expand around the center square from 1970s and the following decades (Figure 3-(B)) (“Amersfoort”, n.d.).

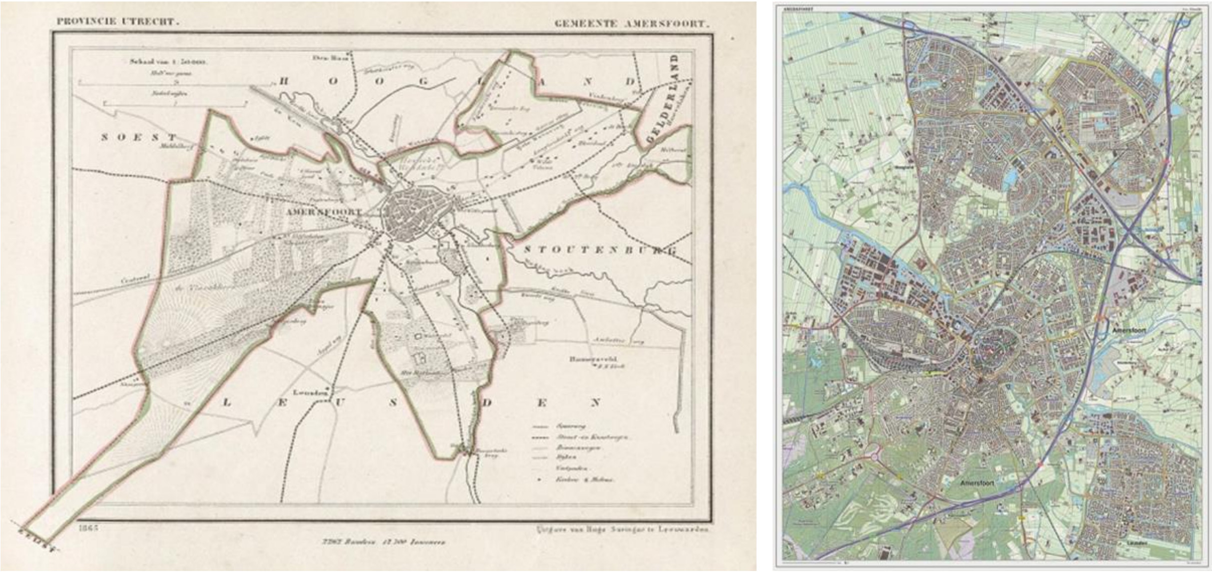

(A) (B)

Figure 3 Maps of Amersfoort in 1985 and 2014. (A): Map from 1865 of municipality of Amersfoort; (B): Map of city area of Amersfoort in 2014 (image acquired date: 22 March, 2014) Source: (A): J. Kuyper. (1870). Gemeente-atlas van Nederland naar officieele bronnen bewerkt; (B): Janwillemvanaalst. (2014). Topografische kaart van Amersfoort.

At present, the total area of Amersfoort municipality is about 63.86 km^2 (Figure 4), consisting of 62.86 km^2 land and 1.00 km^2 water, respectively. Generally, Amersfoort city region can be divided into two parts, the inner city and the modern city. As indicated by Figure 4, the inner city is located in the center part around the canal running through the city. The rest of resident and commercial areas make up the modern city, surrounding the inner city.

Figure 4 Amersfoort city, NL

Source: IPO Luchtfoto actueel of Amersfoort, 2011

The most developed part of Amersfoort was selected to map the impervious surface and a more zoomed-in region of elevated area was employed to examine its runoff responses with respective to the computing constrains and efficiency. A rectangle covering most impervious surfaces in Amersfoort was selected as the study area for impervious areas mapping (Figure 5 ①). The exact location of this study area is described in Table 1. The study area covers a total area of **38.95 km^2**, representing almost **60%** of the whole Amersfoort city. In the study area, several land covers are present, such as resident and commercial buildings, asphalt/concrete roads, bridges, canal, parking lots, bare soil, grass and trees and vegetation.

	X coordinate (m)	y coordinate (m)	
Upper left	660405	5786535	Projection: UTM Datum: WGS-84
Upper right	665235	5786535	
Lower left	660405	5778345	
Lower right	665235	5778345	

Table 1 Corner coordinate values for the study area

Amersfoort city is quite flat except the southern west part where is located besides an elevated hill. Therefore, a more zoomed-in study area for runoff analysis is selected (Figure 5 ②). The only elevated hill is contained in this study area so that the rainfall-runoff response should be more significant in this region.

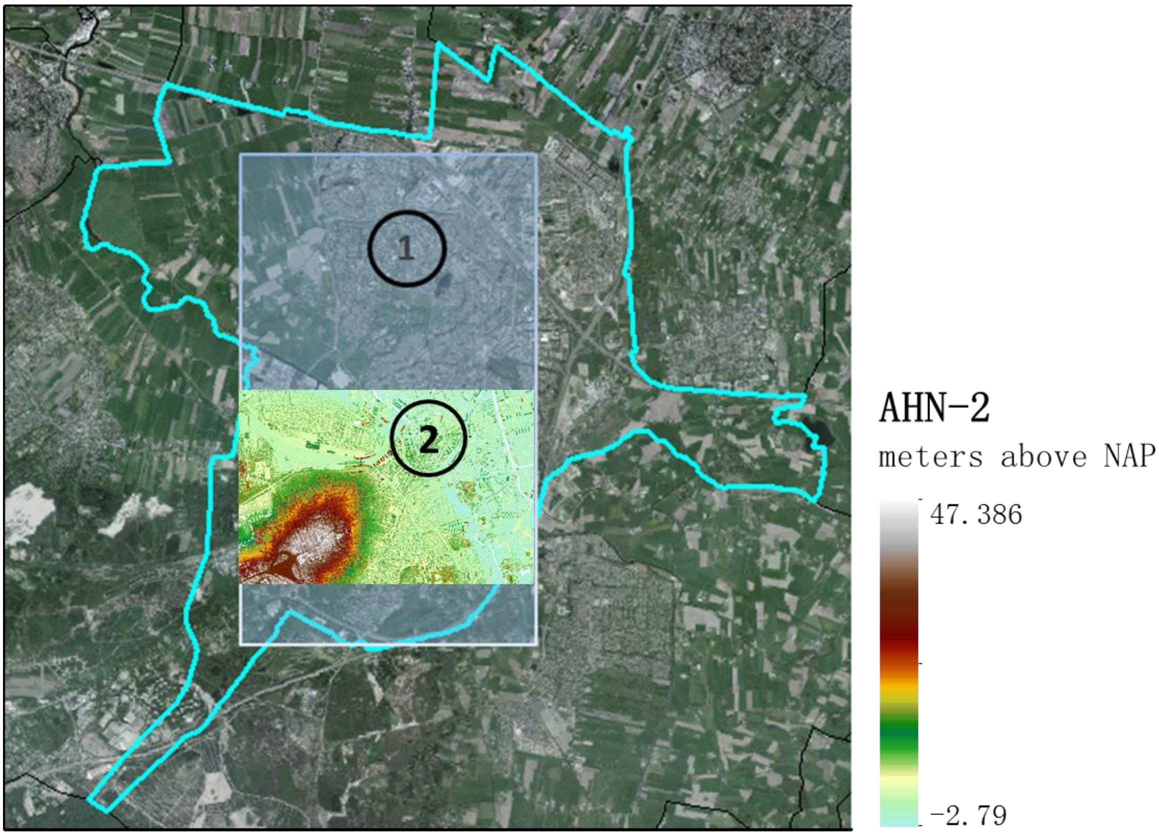

Figure 5 Study area: ①: Study area for impervious surface mapping; ②: Study area for runoff modeling overlaid by AHN-2

Source: IPO Luchtfoto actueel of Amersfoort, 2011; AHN-2, 2012.

Precipitation drives the runoff process so that some basic information on precipitation for Amersfoort is described in the following. Amersfoort has an annual average precipitation (rain and snow) of **739 mm** (*Utrecht Precipitation, www.whether-and-climate.com*). The average monthly precipitation throughout 2013 year is shown in Figure 6. Months from September to November has a bigger amount of average precipitation due to the large volume of rainfall and snow. Months of June and July are also rainy seasons with an average of rainfall of 64mm and 63mm, respectively. Some intensive rainfall events are more likely to happen during these two months.

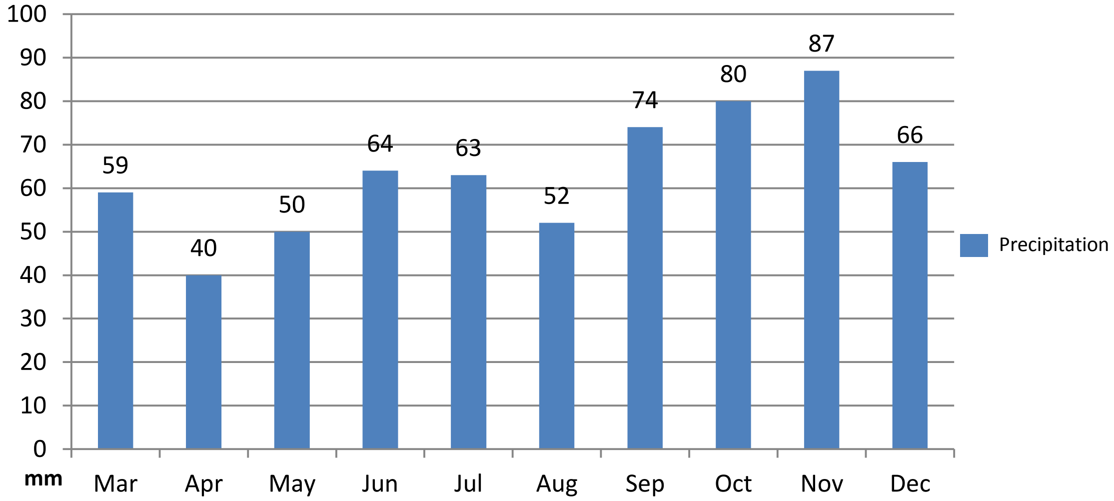

Figure 6 Average monthly precipitations over Utrecht Province in 2013, NL

Source: Utrecht Precipitation, 2013 http://www.weather-and-climate.com/average-monthly-Rainfall-Temperature-Sunshine,Utrecht,Netherlands

The precipitation amount with respective to different rainfall durations and return times is shown in Table 2. Considering a case of one-hour rainfall event, a rainfall of 10 mm/hour can be expected twice a year, while a rainfall of 23mm/h may occur every five year.

Rainfall(mm/hour)	**Minutes**				**Hours**				
	5	15	30	60	2	4	6	8	12
10 x per year	-	3	4	5	7	9	11	12	13
5 x per year	-	4	6	7	10	12	14	15	17
2 x per year	4	6	8	10	13	16	19	20	23
1 x per year	5	9	11	14	17	21	23	24	27
1 x per 2 year	7	11	14	18	21	25	27	29	32
1 x per 5 year	9	15	19	23	26	31	34	36	40
1 x per 10 year	11	18	23	27	31	36	39	41	46
1 x per 20 year	12	21	27	32	36	41	45	47	52
1 x per 50 year	15	26	32	38	42	49	53	56	61
1 x per 100 year	17	29	37	43	48	55	59	62	68

Table 2 Rainfall intensities and durations with respective to different return times.

Source: Buishand A. & Wijngaard, J., (2007). Statistiek van extreme neerslag voor het stedelijk waterbeheer. T*echnical report TR-295, KNMI, De Bilt*.

4 Satellite data preparation

Considering the easy availability and high-quality of data, satellite images of Landsat-4, -5, -7, -8 and FORMOSAT-2 were selected. Care should be taken to ensure that images are of sufficient quality and are cloud- and haze- free for a high-quality information extraction.

4.2 Landsat imagery

Landsat images were selected for impervious surface mapping with respective to the medium spatial resolution. To examine the expansion of impervious area in Amersfoort for the last 30 years, a series of Landsat-4, -5, -7, -8 images acquired on 5th July, 1987, 23th May, 1992, 16th May, 1998, 15th April, 2007 and 9th Mach, 2014 were used. The images have a spatial resolution of 30 meters. Six multi-spectral bands were employed, including blue, green, red, NIR (Near Infrared), SWIR1 (Short-Wave Infrared 1) and SWIR2 (Table 3). Summer images were preferred because Weng *et al.* (2009) found that a summer image performed better for estimation of impervious surfaces than ones in other seasons based on a case study in Indianapolis, U.S.A.

TM (Landsat-4, -5)			ETM+ (Landsat-7)			OLI (Landsat-8)		
Band Number	Band Wavelength	Res. (m)	Band Number	Band Wavelength	Res. (m)	Band Number	Band Waveleng	Res.(m)
						B1- Coastal/Aerosol	433-453	30
B1-B	450-520	30	B1-B	450-515(483)	30	B2-B483	450-515	30
B2-G	520-600	30	B2-G	525-605(565)	30	B3-G	525-600	30
B3- R	630-690	30	B3-R	630-690(660)	30	B4-R	630-680	30
B4-NIR	760-900	30	B4-NIR	775-900(838)	30	B5-NIR	845-885	30
B5-SWI	1550-1750	30	B5-SWI	1550-1750(1650)	30	B6-SWI1	1560-1660	30
B6-TIR	10400-12500	120	B6-TIR	10400-12500	60	B7-SWI2	2100-2300	30
B7-SWI2	2080-2350	30	B7-SWI2	2090-2350(2220)	30	B8-PAN	500-680	15
			B8-PAN	520-900	15	B9-Cirrus	1360-1390	30

Table 3 Band information for Landsat sensors. R: red, G: green, B: blue, NIR: near infrared, SWIR: short-wave infrared, PAN: panchromatic;

Source: Landsat Science, 2014. Retrieved from http://landsat.gsfc.nasa.gov/?page_id=9

All the images (path: 198, row: 24) were downloaded according to the WRS (World-wide Reference System) from the EROS Glovis site (*http://glovis.usgs.gov/*). Figure 7 shows an example of Landsat 8 image for study area acquired on 9th March 2014 in composition of NIR, red, green.

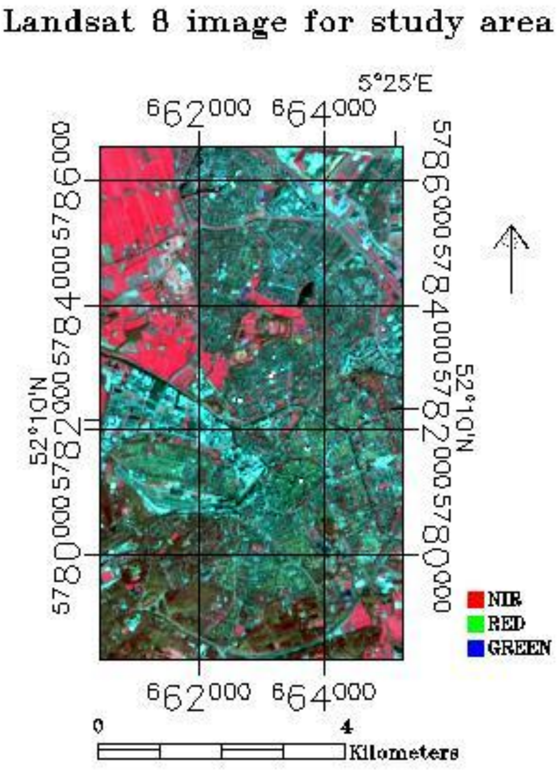

Figure 7 Landsat 8 image for study area in composition of NIR, red and green.

4.2 FORMOSAT-2 imagery

The image of FORMOSAT-2 satellite has one panchromatic band and four multispectral bands, composing of blue, green, red and NIR (Table 4). The resolutions of the multispectral and panchromatic bands are up to 8 meters and 2 meters, respectively. It can provide high spatial resolution imagery containing much richer information than Landsat satellites. One image acquired on 22nd July in 2013 was downloaded with authorization. The FORMOSAT-2 image of study area in composite of false color is shown in Figure 8.

FORMOSAT-2		
Band Number	**Band Wavelength (nm)**	**Resolution (m)**
B1-B	450-520	8
B2-G	520-600	8
B3-R	630-690	8
B4-NIR	760-900	8
PAN	520-820	2

Table 4 Band information for FORMOSAT satellite sensor.

Source: FORMOSAT-2, 2014. Retrieved from http://www.geo-airbusds.com/en/160-formosat-2

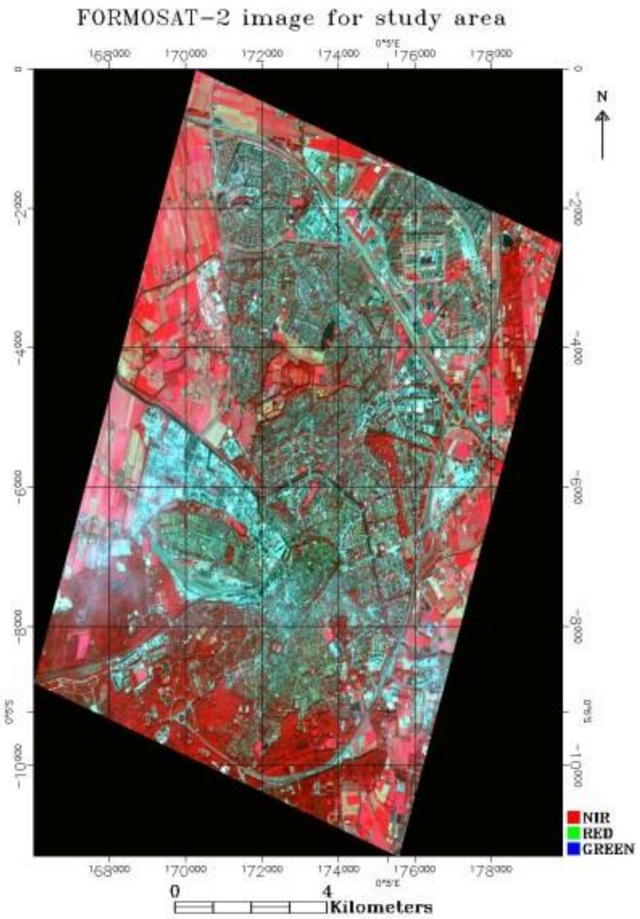

Figure 8 FORMOSAT-2 image for study area in false color

5. Methods

This chapter describes the applied methods for impervious surface mapping and runoff modeling.

5.1 Impervious surface mapping

Three widely-used approaches for impervious surface mapping were selected and applied to Amersfoort. Two approaches, regression modeling and Normalized Linear Spectral Mixing Analysis (NLSMA) were applied to medium spatial resolution images (Landsat images) and the third, the Decision Tree Classification (DTC) approach was used for images with high spatial resolution (FORMOSAT-2 images).

5.1.1 Regression modeling approach with Landsat 8 images

Flowchart 1 illustrates the procedures for the regression modeling approach. The key steps are image acquisition, land cover classification, development of a regression model, application of the regression modeling and accuracy assessment. These key steps are described in the following.

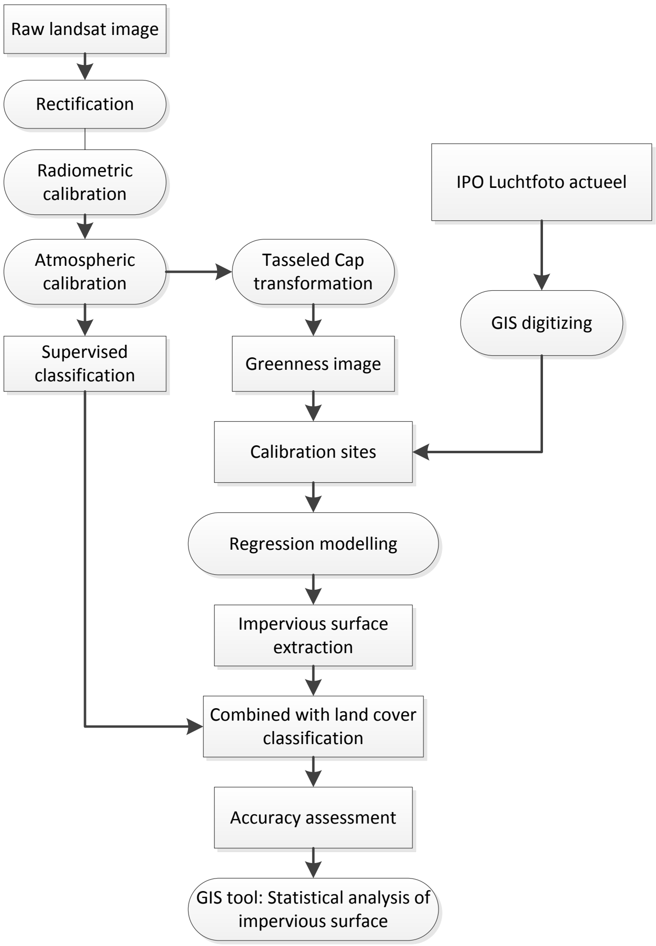

Flowchart 1 Image-processing procedures for the regression modeling approach

① Landsat Image acquisition, rectification and land cover classification

Rectification is required to make sure that all the images are projected to the same coordinates and projection (Weng, 2008). Rectification ensures that all images are in seamless continuity if a large area is investigated. At this stage, the study area is rectified to the UTM (Universal Transverse Mercator) coordinate and projection system based on WGS-84 (World Geodetic System) datum.

It is much more efficient to block out the non-urban areas and apply the regression modeling only to the urban areas. In the study area, pervious surfaces, such as forest and grassland, are mainly found in non-urban areas whereas impervious surfaces, such as buildings, asphalts roads are predominantly restricted within the urban areas. A mask of non-urban areas was created after performing classifications on the original images. Various classification methods like supervised classification (e.g. Maximum Likelihood Classification) and unsupervised classification are available. Based on the classification scheme of the Anderson classification system (Anderson *et al.* 1976), five classes including **agriculture**, **forest**, **residential area**, **commercial area** and **water** were used to describe the landscape of the study area. Fractions of agriculture, forest and water were regrouped into the non-urban area, which was blocked out for further analysis.

② Development of impervious surface regression modeling

The greenness used in developing the regression model was calculated by tasseled cap transformation (Crist and Cicone, 1984), which is an orthogonal transformation of reflective band data. Three components were derived after transformation, among which the first component –brightness- is related to the amplitude of reflectance associated with soils and impervious areas, the second component –greenness- is orthogonal to brightness and is strongly related to the amount of green vegetation while the third component –yellowness- is interpreted as an index of soil or surface moisture.

The relationship between greenness and impervious surface percent was determined from 70 random AOI (Area of Interest) samples, listed in Appendix I. For each sample, a pair of values of the greenness and actual impervious surface percent was recorded. The actual imperviousness percent value in each pixel of an image is measured and calculated visually based on the aerial-view image (Figure 9-(B)). The pixel in the Figure 9-(A), outlined in red, is an example of an AOI sample with its corresponding place shown in Figure 9-(B). The impervious surface percent was estimated as 35%, which was related to a greenness of -0.1017.

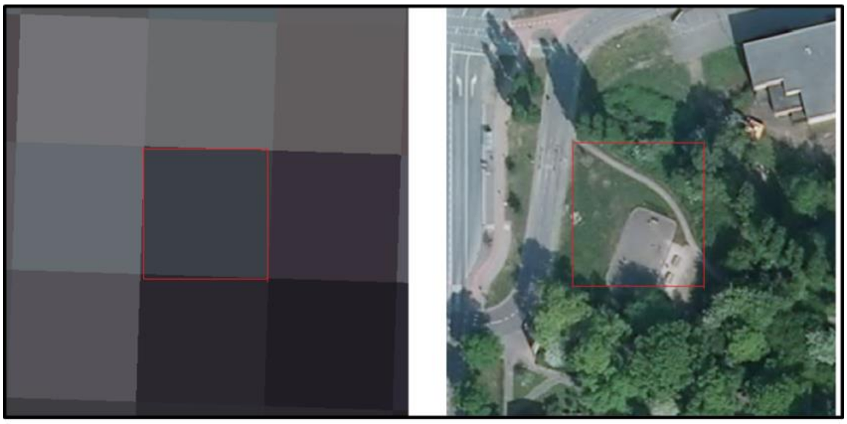
(A) (B)

Figure 9 An example of samples. (A): greenness of the rectangle: -0.1017; (B): measured imperviousness percent: of the rectangle: 35%)

Source: IPO Luchtfoto actueel (2011).

A least squares regression trend line relating percent of impervious surface areas to the value of greenness was determined from these 70 samples. Figure 10 illustrates the mathematical relationship between them. A second order regression trend line was determined. An R^2 of **0.86** forms a solid foundation on which to prove the strong relationship between greenness and percent of impervious surface area.

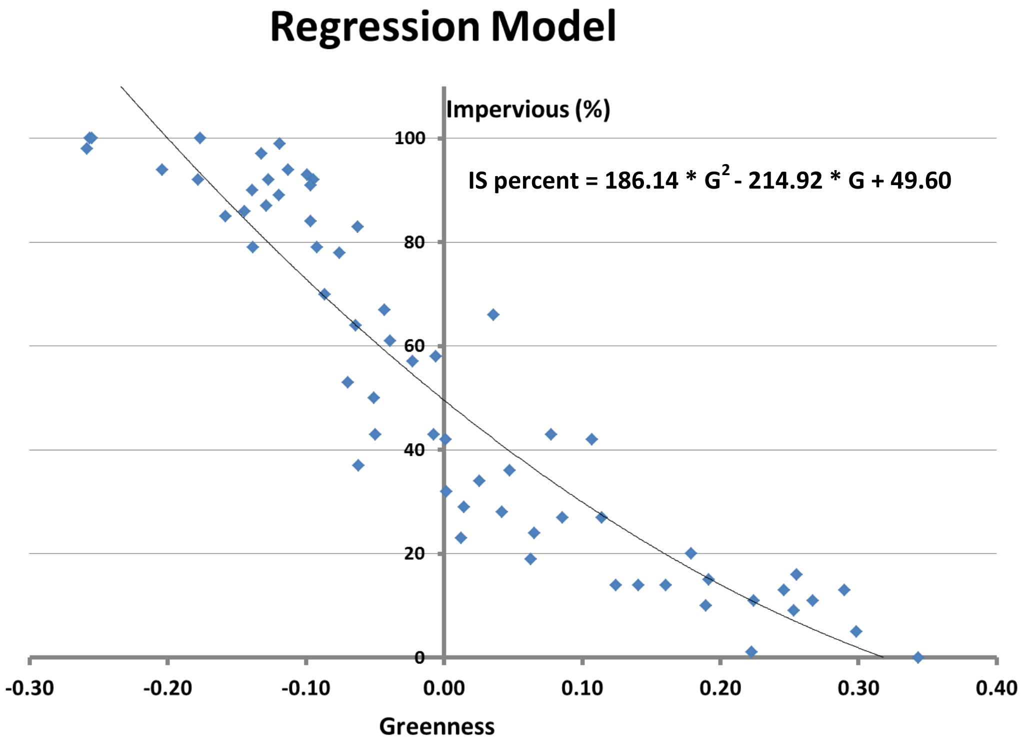

Figure 10 Relationship between Tasseled Cap Greenness and visual estimated impervious surface percent, (N = 70, R^2 = 0.86)

③ Impervious surface extraction

The impervious surface was mapped by applying the regression model equation to the greenness fraction image for the entire urban study area. A final check of maximum and minimum imperviousness percent value was required because the impervious surface percent derived from a regression model may be less than 0% or more than 100%, which should be rectified to 0% and 100%, respectively.

④ Accuracy assessment

Accuracy assessment followed in order to evaluate how well the regression modeling approach mapped the impervious surface area.

110 samples that were not used to develop the regression models were selected, balanced across the study area (Appendix II). The estimated percent of impervious surface area was plotted against the measured percent. The fitness between them can be evaluated by R^2.

The accuracy was also evaluated by two statistical indices: RMSE (root-mean-square-error) and SE (systematic error). The equations used for these calculations are shown in Equation (1) and (2), respectively (John C. Davis, Statistics and data analysis in Geology (3rd edition)):

$$\mathrm{RMSE} = \sqrt{\frac{\sum_{i=1}^{N}(\widehat{V_i} - V_i)^2}{N}} \tag{1}$$

$$\mathrm{SE} = \frac{\sum_{i=1}^{N}(\widehat{V_i} - V_i)}{N} \tag{2}$$

Where $\widehat{V_i}$ is the estimated percent impervious value for sample i; V_i is the measured percent impervious value for sample i; and N is the total number of samples. RMSE measures the overall estimation accuracy for all samples. A result with a low RMSE performs better than that with a high RMSE. An SE over zero indicates an overestimation and vice versa.

These accuracy statistics (i.e. RMSE values and SE values) can be used not only for evaluating a single approach, but also offer a solid basis for comparison between various approaches. This accuracy assessment strategy will also be used to evaluate the performance of the NLSMA approach.

5.1.2 Normalized LSMA approach with Landsat Images

Flowchart 2 shows the procedure for the NLSMA approach. Landsat images rectification have already been explained in the regression modeling approach. Therefore, emphasis is placed on the portion of the procedure from radiometric calibration to accuracy assessment.

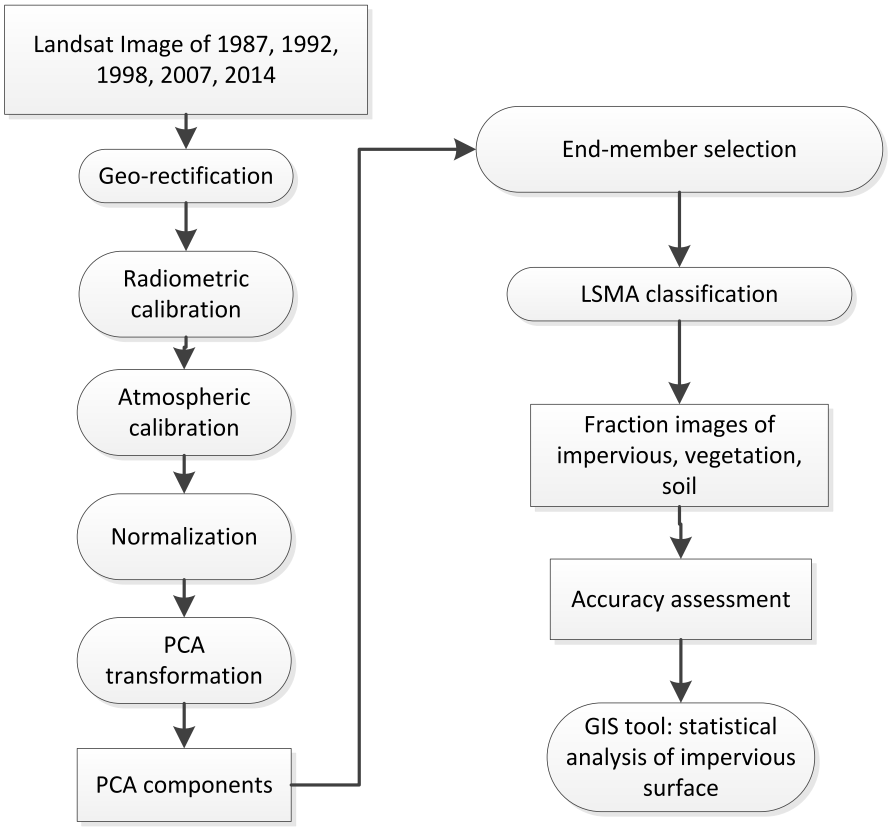

Flowchart 2 Image-processing procedures for NLSMA

① Radiometric calibration

NLSMA finds factions of various land covers (referred to as end-members) making up a pixel by separating the pixel spectrum into several reference spectrums. To achieve this, the reflectance spectrums of the pure land covers are required. However, due to the atmosphere effect (scattering effect) and the sensor itself, the radiance detected by the TM (or ETM+) sensor is not exactly the same as the amount of radiance reflected by the objective materials. Therefore, before applying NLSMA, it is necessary to make a radiometric correction that converts the digital number of the raw radiance image into exo-atmosphere reflectance. Radiometric correction and quick atmosphere correction in ENVI were used for this process.

② Brightness variation in spectrums and the normalization process

The real landscapes are much complicated, involving far more than three basic types of land covers (impervious surface, vegetation and soil). Moreover, for a single type of land cover, the objects and their spectral features can be quite various. Two examples are given in Figure 11. Figure 11-(A) and -(B) illustrate the spectral variation of vegetation and impervious surfaces, respectively. From these two spectral features, it can be seen that the brightness variations are significant. For vegetation, a significant variation is observed at band 4 (NIR). The bright vegetation (such as green crops) has a reflectance of 37% while dark vegetation (such as dense forest) is only 14%. The variation in vegetation is closely-related to the variations in water content and leaf chlorophyll. The brightness variation is much more in impervious surfaces because the spectrums of impervious surfaces can range from very low albedo (e.g. asphalt roads) to high albedo (e.g. manmade plastic materials). The most significant variation in reflectance (brightest: 47%, darkest: 14%) occurs at band 3 (Figure 11-(B)). This is mainly due to the various kinds of materials human beings use for different types of constructions, such as buildings, houses and roads. Similarly, soil also has a variation in spectral feature mainly due to soil's variability in composition and structure.

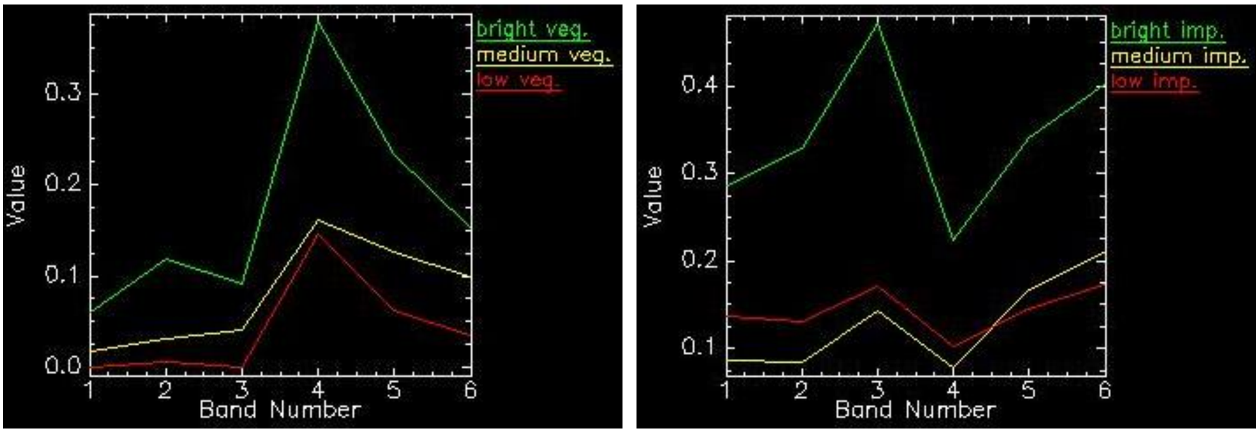

(A) (B)

Figure 11 Spectral variation of vegetation and imperious surface. (A): vegetation; (B): Impervious surface

Great brightness variations in a single type of land cover can cause problems, such as difficulty in selecting endmembers (Wu, 2004). Wu (2004) has shown that a pure urban land cover not only exists around the vertexes of the points cloud in a scatter plot, but also scatters along the edges of the point clouds (such as land covers of dark or medium brightness impervious areas).

Under these circumstances, a normalization procedure, proposed by Wu (2004), aimed at reducing brightness variation was applied in our analysis. The normalization equation is given in Equation (3) and (4) (Wu, 2004):

$$\overline{R_b} = \frac{R_b}{m} * 100 \tag{3}$$

$$\mathrm{m} = \frac{1}{N} \sum_{b=1}^{N} R_b \tag{4}$$

Where $\overline{\mathrm{R_b}}$ is the normalized reflectance for band b in a pixel; R_b is the original reflectance for band b; m is the average reflectance for that pixel, and N is the total number of bands. Figure 12 illustrates the spectral features of vegetation and impervious surfaces for the same pixels as those shown in Figure 11. The reflectance values of vegetation and impervious surfaces changed after normalizing the original reflectance to the average reflectance of a pixel. It can be seen that the significant variations in brightness, particularly in band 4 of the vegetation spectrum and band 3 of the impervious surface spectrum, are reduced although the variations in other bands remain the same. After normalization, three single land cover types (impervious surface, vegetation and bare soil) can be used to describe the urban landscapes and map the impervious surface area.

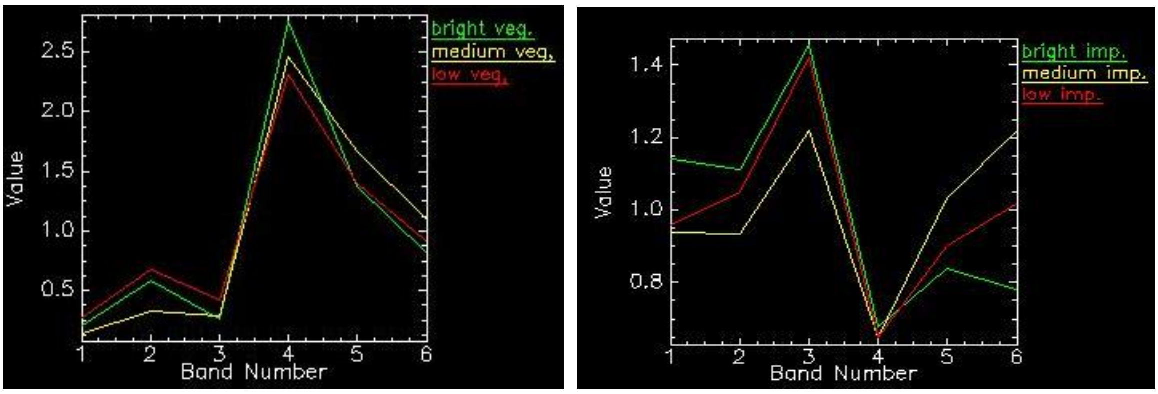

(A) (B)

Figure 12 Spectral variation of vegetation and impervious surface after normalization. (A): Vegetation; (B): Impervious surface.

Figure 13 illustrates the Landsat 8 original and normalized reflectance images with a composition of NIR, red and green. Visually, the differences between vegetation and forest, between commercial and residential areas were minimized after normalizing. It could be argued that the minimization of spectra variation may disable the ability to distinguish different land objects in detail but, considering that the focus is laid on extraction of impervious surfaces, this and other redundant information can be ignored. So the redundant information was dismissed while only the most important land cover types (impervious surfaces, vegetation and soil) were separated.

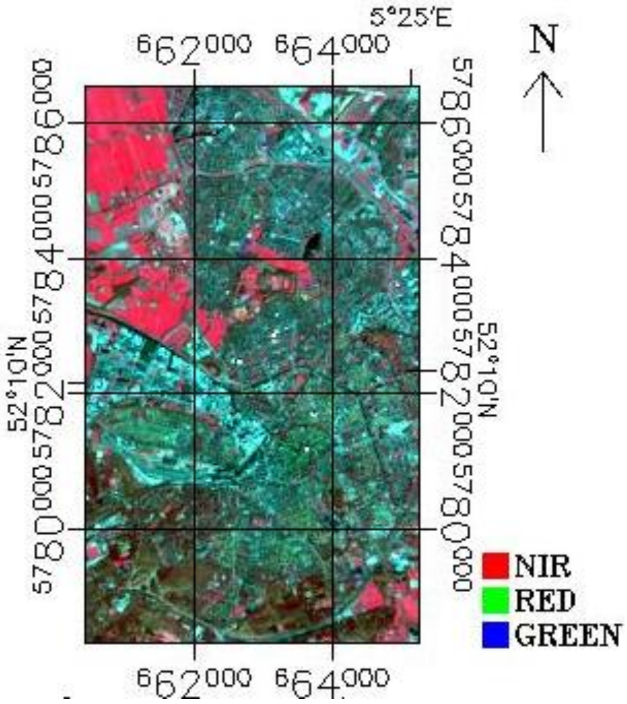

(A)

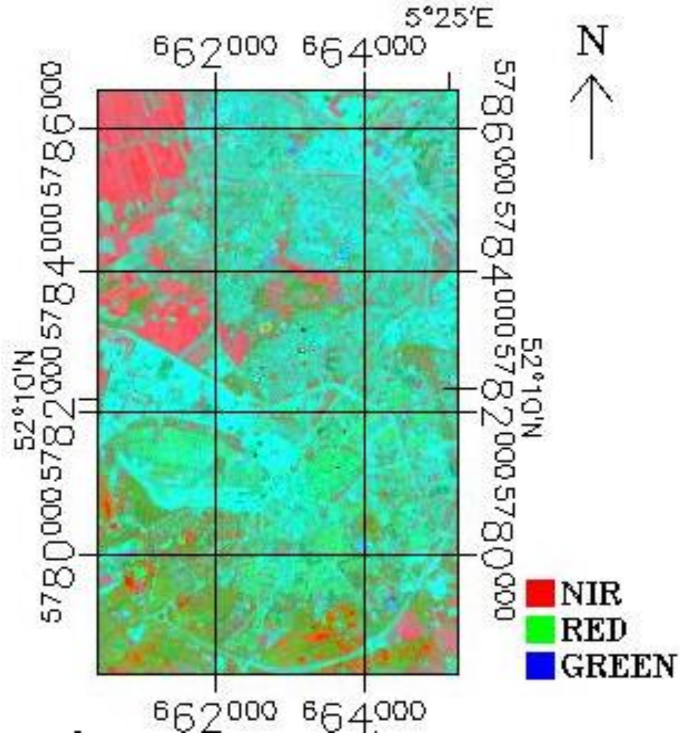

(B)

Figure 13 Comparison between original and normalized Landsat 8 image. (A): Original image; (B): Image after normalization.

③ PCA (Principle Component Analysis) transformation and endmember selection

PCA transformation followed to minimize band correction and guide endmember selection. Normally, after applying the PCA, the first three or four components are the most valuable because they contain almost all of the information in the image while the other components are filled with noise and can be dismissed. Table 5 gives information about the eigenvalues of the principle components. The first three components describe 96% of the total variances and these first three PCA images are shown in Figure 14. After applying PCA transformation, the spectral scatter plots (spectral feature spaces) were created and can be employed to select endmembers (Figure 15).

Eigenvalue Number	**Eigenvalue**	**Cumulative percent**
1	3.786	63.11%
2	1.363	85.83%
3	0.611	96.02%
4	0.157	97.34%
5	0.081	98.98%
6	0.000	100.00%

Table 5 Eigenvalues of principle components

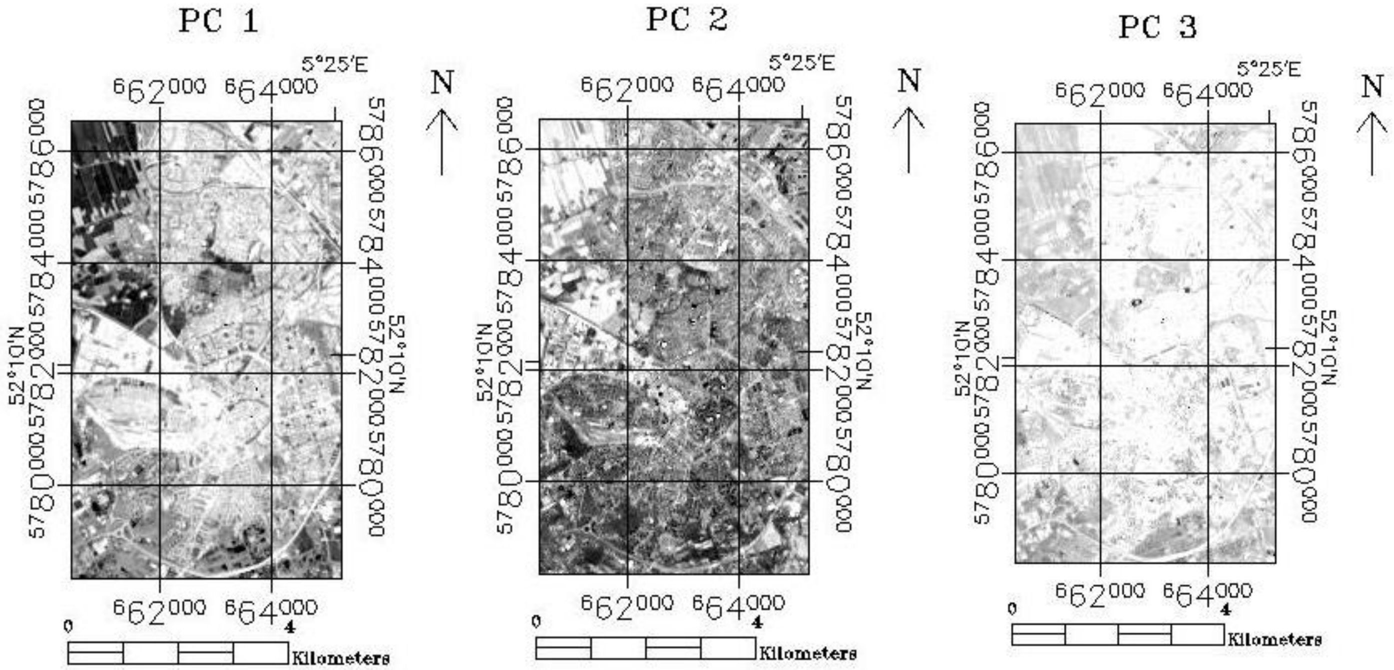

(A) (B) (C)

Figure 14 Images of principle component 1, 2 and 3. (A): Image of PC1; (2): Image of PC2; (3): Image of PC3

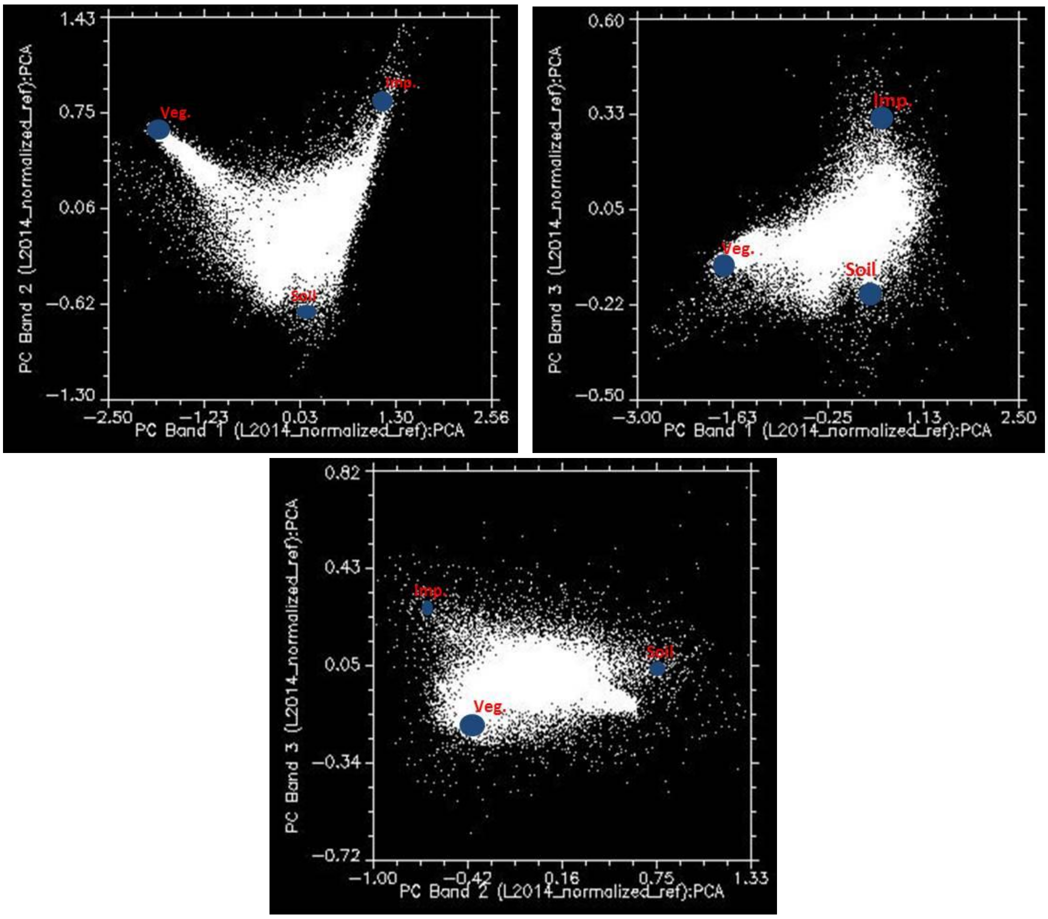

Figure 15 3 spectral feature spaces with different combinations of principle components 1, 2 and 3.

④ Impervious surface extraction by NLSMA

Equation (5) is the linear spectral mixture model (Ben Somers *et al.*, 2011):

$$R_b = \sum_{i=1}^{N} f_i R_{i,b} + e_b \tag{5}$$

where R_b is the reflectance for each band, N is the number of end-members, f_i is the fraction of end-member, $R_{i,b}$ is the reflectance of end-member i for band b, and e_b is the residual. Constraints of $\sum_{i=1}^{N} f_i = 1$ and $f_i > 0$ are required and a single set of numerical solutions can be solved. The linear spectral separation was accomplished via mapping methods that is available in ENVI.

⑤ Accuracy Assessment

The accuracy assessment scheme for NLSMA is exactly the same as that in regression modeling. In order to make a comparison with the result of regression modeling approach, the same amount of samples (110) was selected. The accuracy indices (RMSE and SE) were also calculated and compared to the RMSE and SE of the regression modeling approach.

5.1.3 DTC approach with FORMOSAT image

Flowchart 3 illustrates the Decision Tree Classifications (DTC) (Goetz *et al.*, 2003). The key steps are spectral signatures enhancement, analysis and the decision tree construction.

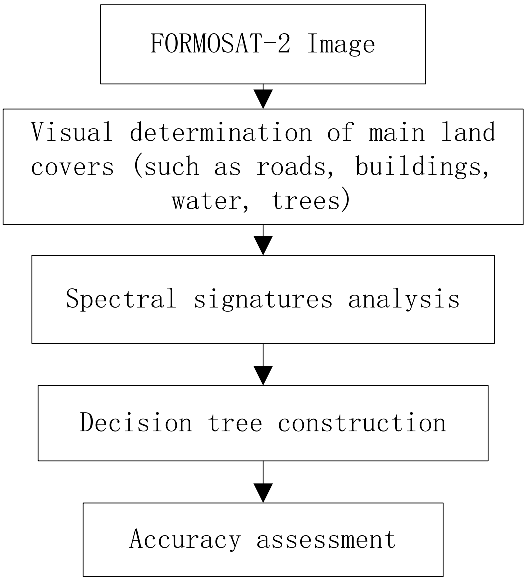

Flowchart 3 Image-processing procedures for DTC

① Spectral feature enhancement

The spectrum of raw FORMOSAT-2 imagery comprises only four multispectral bands (R, G, B and NIR.). Figure 16-(A) shows the spectral signatures of six different land covers: vegetation, forest, rooftops, roads, water and soil. It is clear that bands 1, 2 and 3 are highly correlated with each other and it seems hard to distinguish various land objects using only these four bands.

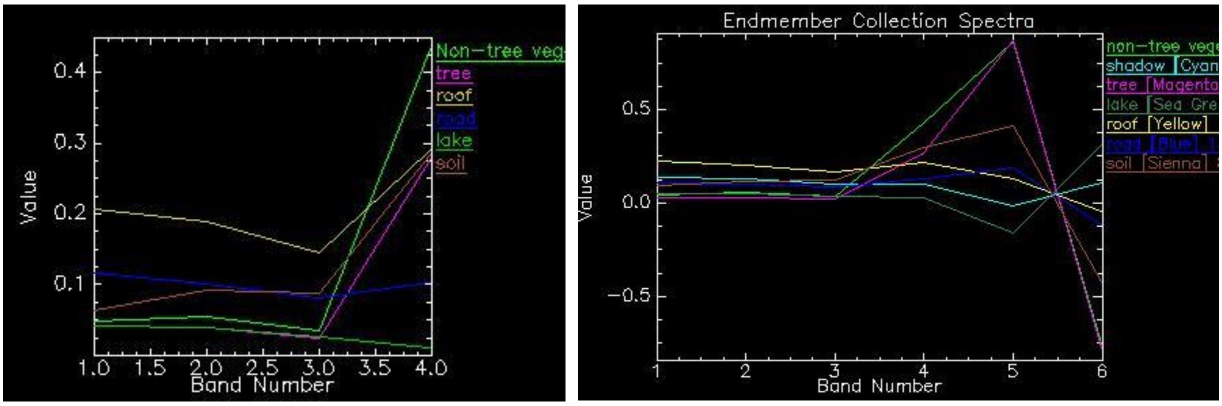

(A) (B)

Figure 16 Comparison between original spectral space (A) and enhanced spectral space (B)

In order to enhance the spectral feature performance, two additional indices, the Normalized Differential Vegetation Index (NDVI, Equation 6) (Samuel *et al.*, 1991) and the Normalized Differential Water Index (NDWI, Equation 7) (Gao, 1996) were added to the spectral features as bands 5 and 6, respectively. By adding these two bands, at least two advantages can be expected: ① NDVI and NDWI show either low or negative correlation with the four original bands, which will reduce the redundancy of the image data and make it more separable. ② Non-impervious surface area is mainly composed of water, vegetation and soil. The addition of NDVI- and NDWI- derived bands can help to separate water and vegetation from soil efficiently (Goetz *et al.*, 2003). Figure 16-(B) illustrates the enhanced spectral features and shows that after spectral enhancement, bands 4, 5 and 6 provide sufficient information to help separate different land objects. Therefore, the 6-band feature spectrum was used to construct the decision tree (Pal & Mather, 2003).

$$\mathrm{NDVI} = \frac{(B4-B3)}{(B4+B3)} \tag{6}$$

$$\mathrm{NDWI} = \frac{(B2-B4)}{(B2+B4)} \tag{7}$$

② Spectral signature analysis and decision tree construction

To construct the decision tree, a rule should be generated that specified threshold for separating various land covers. In this case, all the thresholds were determined by analyzing the statistical features of the training samples. Five land covers classes were selected for the spectral analysis: tree, non-tree vegetation, rooftops, road and soil. Trees are shown in dark red while non-tree vegetation is shown in bright red in the false color images. These five classes were then grouped into the three land cover types that we are concerned with: impervious surface, vegetation and soil. Water body was masked by screen digitizing because only a very small amount of water was present in the study area.

Pal and Mather (2003) concluded that the accuracy of the DTC approach is related to the size of the samples therefore, around 1000 pixels for each class were selected with care to make sure each type of land cover contains a good amount of samples. The spectral signatures for the five classes are shown in Figure 17 and the mean values of the reflectance of these five classes are given in Table 6.

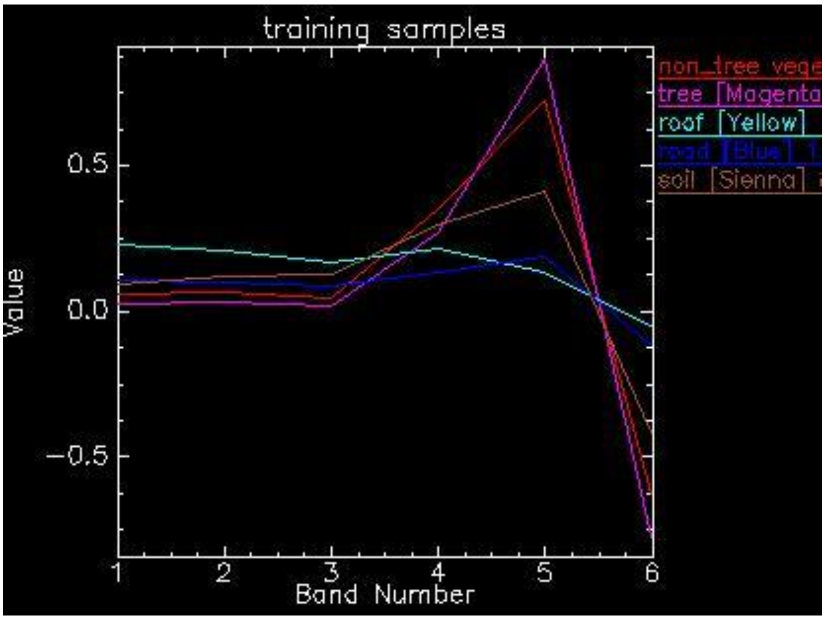

Figure 17 Average spectral signatures for training samples

Classes	**Sub-classes**	**B1**	**B2**	**B3**	**B4**	**B5(NDVI)**	**B6(NDWI)**	***B4/B3***	***-(B6/B5)***
Vegetation	Non-tree veg	0.04180	0.05783	0.03318	0.43356	0.85923	-0.76724	*13.07*	*0.89*
	Tree	0.02714	0.02890	0.01850	0.26735	0.86757	-0.80221	*14.45*	*0.92*
Impervious surface	Roof	0.22662	0.20598	0.16644	0.21716	0.13267	-0.04777	*1.30*	*0.36*
	Road	0.10945	0.10261	0.08821	0.13135	0.19114	-0.11832	*1.49*	*0.62*
Soil	Soil	0.09163	0.11897	0.12516	0.29925	0.41064	-0.43156	*2.39*	*1.05*

Table 6 Average value of reflectance for training samples

By exploring Table 6, two rules can be concluded:

① vegetation has a higher reflectance in band 4 (NIR) while the value of band 3 is much lower than other classes;

② Impervious surfaces have a higher NDWI value and a lower NDVI value than soil.

The division between band 4 and band 3 can be used to separate vegetation based on rule ①; The value of - (B6/B5) can be used to distinguish soil from impervious surface because this value is larger than 1 only for soil. Therefore, a decision tree can be constructed as follows (Figure 18). The threshold of **3.7** and **2.0** are optimized by several trials.

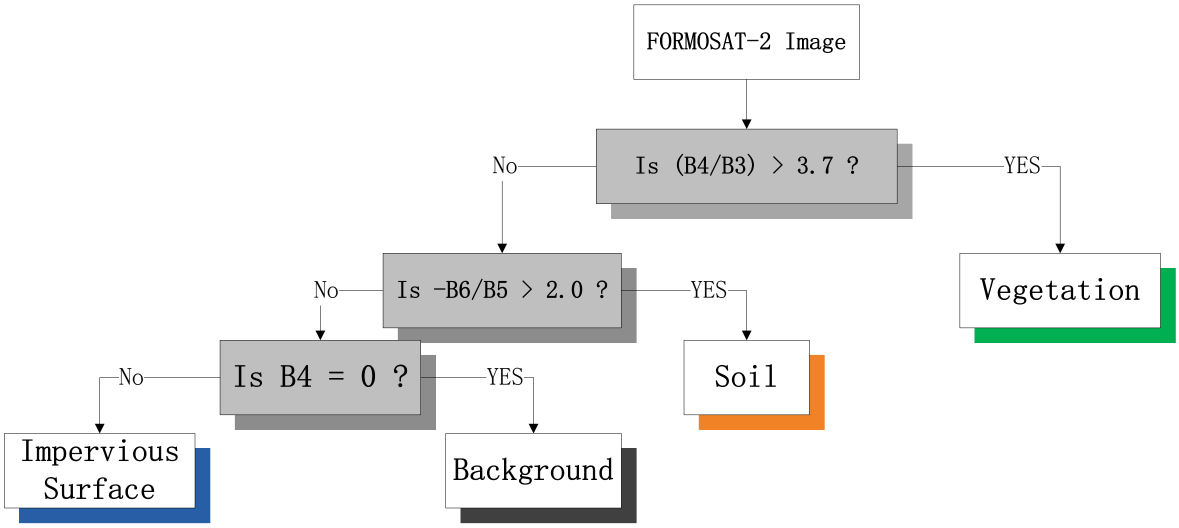

Figure 18 Decision tree used for impervious surface mapping

③ Accuracy assessment

The method used for accuracy assessment of DTC is different from the methods used for medium resolution images. In this case, the **error matrix** and **KAPPA analysis** (Fitzpatrick Gerold, 1986; Russel, 1991) will be used for accuracy assessment of the DTC. The error matrix, also known as the confusion matrix that is used to test whether the pixel in the image is correctly classified based on the reference data on the ground. In the error matrix, several indexes such as producer's accuracy, user's accuracy and overall accuracy are to be used to present obtained accuracy. KAPPA is another index to evaluate the agreement between two input images. It ranges from -1 to 1. If the two input images are exactly the same, then the KAPPA is 1. On the other hand, if they are completely different, then KAPPA has a value of -1. Landis and Koch (1977) described agreement measures for categorical data, as illustrated in Table 7. More knowledge about accuracy assessment of classification of remotely sensed data can be found in Russell (1991).

KAPPA statistics	Strength of agreement
<0.00	Poor
0.00-0.20	Slight
0.21-0.40	Fair
0.41-0.60	Moderate
0.61-0.80	Substantial
0.81-1.00	Almost Perfect

Table 7 Strength of agreement indicated by KAPPA

Considering the focus of this study is on impervious surface accuracy, vegetation and soil fractions were combined into a single group – the pervious surface group. A minimum of 300 samples for each land use category in the error matrix were collected for a reliable assessment. The sample scheme was conducted randomly, and great care was taken to ensure little or no bias was involved.

5.2 Runoff modeling analysis

5.2.1 Runoff model

The simple rainfall-runoff model used in this study was constructed based on the knowledge described in the theoretical background. It was a modified version of the simple rainfall-runoff model provided by the PC Raster team of Utrecht University (www.pcraster.geo.uu.n). This model is particularly appropriate for the simulation of the extent and location of runoff in a watershed or an elevated area. The model construction is presented in Flowchart 4. Three key components were integrated: precipitation, infiltration and local terrain. For every calculation loop, the water surplus on the ground can be calculated by subtracting the net rainfall data by the infiltration capacity. Combined with local drain direction derived from DEM (Digital Elevation Model), the surface runoff can be determined for each time-step. By repeating this process, a dynamic rainfall-runoff model is constructed. At the end of every time step, the desired results are reported with, for example, a map with discharges of water or with runoff depth above the ground.

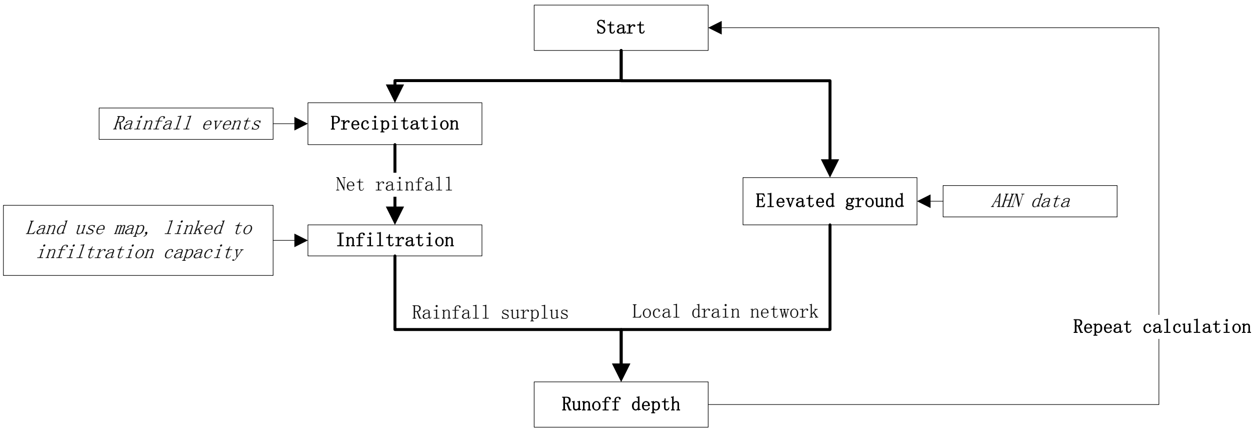

Flowchart 4 Runoff model description

Inputs for the basic hydrological model are the rainfall data, land cover and DEM (digital elevation model) maps. Rainfall data can be selected from history rainfall events for Amersfoort. The impervious surface map can be employed as land cover data. AHN-2 (2012) can provide the local DEM data at various resolutions.

5.2.2 Runoff increase with IS changes

The model was first used to examine how the runoff increases respective to the increasing impervious surface area in Amersfoort. To evaluate the differences, the model was run twice using impervious surfaces maps of 1987 and 2014 while the other setups were kept consistency.

Two impervious surface maps for Amersfoort were used, one from 1987 and one from 2014. Corresponding to the 30 meters resolution of land covers maps, the DEM was also kept at 30 meters by resampling from the 5 meter AHN-2 data (2012).

To quantify the runoff increase, the precipitation has to be the same. A real rainfall event which occurred on June 3, 2008 (KNMI, 2010) was selected for simulation. One reason for selecting this real event is that the rainfall intensity was extremely high for the Netherlands--up to 21.4mm/hour (refer to Table 2). As a result, a significant runoff response can be expected. Another reason is that this rainfall event was uniformly distributed in the south–western part of Amersfoort, which is exactly the area under study here. A uniformly distributed rainfall event can make the runoff response comparison much more straightforward. Other extreme rainfall events that have occurred in Amersfoort are listed in Appendix VI.

For the purpose of examining the increase of runoff due to the increase of impervious surfaces, four land categories derived by NLSMA mapping method, describing the impervious surface percent-- none IS, low IS, medium IS and high IS—were used as land cover map. To determine an infiltration capacity for each of them, the infiltration capacity values from a comparable study by Siebelink (2011) was consulted. Table 8 shows a comparison between the infiltration capacity values used in these two studies and Table 9 contains a summary of the runoff simulation model parameters.

Infiltration capacity (mm/h)		Infiltration capacity (mm/h) in this study	
Buildings	0	None-IS	70
Paved area, paved road	2 – 6	Low-IS	20
Unpaved roads	10	Medium-IS	10
Unpaved area, nature	100	High-IS	3
Remaining, semi-paved	7 – 20		

Table 8 Comparison of land cover infiltration capacity used in Siebelink (2011) and this study

Model setups		
Time-step	1 hour	
Rainfall intensity	21.4mm/hour	
Rainfall duration	1 hour	
Land cover maps	Impervious surface of 1987 and 2014	
Infiltration capacity	Non-IS	70 (mm/h)
	Low IS	20 m/h
	Medium IS	10 mm/h
	High	3 mm/h

Table 9 PCRaster runoff simulation model parameters

5.2.3 Spatial runoff patterns

Runoff modeling at a resolution of 30 meters cannot illustrate the detail spatial runoff patterns on the street due to the coarse image resolution. Therefore, runoff modeling with a high spatial resolution (5 meters) inputs was accomplished to show the runoff patterns on the street. Several scenarios with different rainfall intensities were worked out and their spatial runoff patterns derived.

Table 2 shows the rainfall amounts for various rainfall intensities with different recurrence frequency in the Netherlands. Since only a storm situation was concerned with, the rainfall duration was kept consistent at 1 hour. Four rainfall events with intensities of 10, 14, 18 and 23 mm/hour were used as the precipitation input for the runoff model. The return period for these four rainfall event is **half a year, one, two and five years**, respectively.

Delineating the spatial runoff patterns in urban area requires relatively high-resolution DEM. High resolution elevation model data can reveal the landscape in a more detail way than an elevation model with a low or medium resolution such as 30 meters. Therefore, a DEM with a 5-meter resolution, resampled from the original AHN-2 lidar terrain points (2012), was used for the runoff model (Figure 19).

The high-resolution impervious surface map produced by DTC was selected as the land cover input map. It contained four main land cover types: water, vegetation, soil and impervious surface. It had a spatial resolution of 8 meters so the map can be linked to the runoff model as a land cover map. For perfectly fitting the DEM data, a resampling process converting the original map to a map with 5 meter resolution was performed.

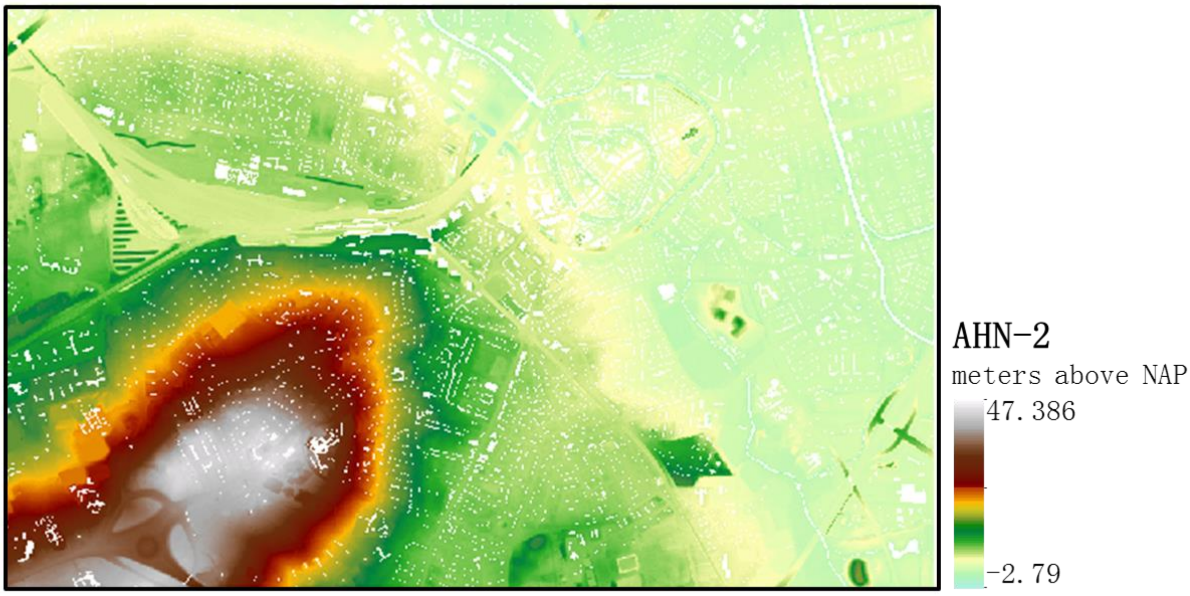

Figure 19 5-meter AHN-2 for runoff modeling.

Source: AHN-2 (Actueel Hoogtebestand Nederland), (2012).

5.2.4 Risk map for buildings

City managers and the government are mostly concerned with which buildings are most vulnerable for potential flooding and how severe the outcome of flooding would be. For this purpose, a straightforward risk map is sufficient and it is possible to make risk maps as preferred as long as the infrastructure properties are available.

A detailed description of the building information in Amersfoort was available (Esri Nederland, Kadaster (BAG), 2014). Table 10 illustrates some main properties that will be used as for creating risk maps.

Properties	Attributes	
Building finished Time (year)	Earliest: 1300	Latest: 2014
Status	Construction started	
	Planning permission granted	
	Buildings for outdoors	
	Building demolished	
	Building in use	
	Demolition license	
	Unrealized property	

Table 10 Properties of buildings used for risk map of buildings.
Source: Esri Nederland, Kadaster (BAG), 2014

The criteria used for creating a spatial distribution of buildings at risk need to be specified. We begin by assuming that a building located closer to the runoff process is at higher risk. Therefore, the first criterion is the distance between the buildings and the runoff flow. In addition, the well-being of a building is a crucial factor that needs to be taken into account. It is assumed that protecting an older building from a runoff process is more urgent. In addition, the status of a building also needs to be considered. The buildings in use and for outdoor activities have the highest protection priority. Table 11 gives a summary of the criteria used for determining building risk distribution, with the risk level described by A (highest), B, C and D (indicating safety).

Risk Level	Distance (meters)	Built Time (year)	Status
A	D<10	Y<1985	● In use ● For outdoor ● Construction started
B	D<10	1985<Y<2104	● In use ● For outdoor ● Construction started
C	10<D<20	All	● In use ● For outdoor ● Construction started
D	20<D<50	All	All

Table 11 Criteria that used for creating maps of risk buildings
Source: Esri Nederland, Kadaster (BAG), 2014

Four different rainfall intensities of 10, 14, 18 and 23 mm/hour were used to map the distribution of buildings at risk in Amersfoort.

6. Results

Results for impervious surface areas mapping and runoff modeling are presented in this chapter.

6.1 Impervious surface mapping

6.1.1 Regression modeling approach with Landsat 8 imagery

The results of supervised classification and the mask map are shown in this section. Five land covers types were identified and classified as agriculture, forest, residential area, commercial area and water. The classification result is present in Figure 20-(A). Figure 20-(B) shows a masked map of the non-urban area by combining commercial and residential area as the urban area.

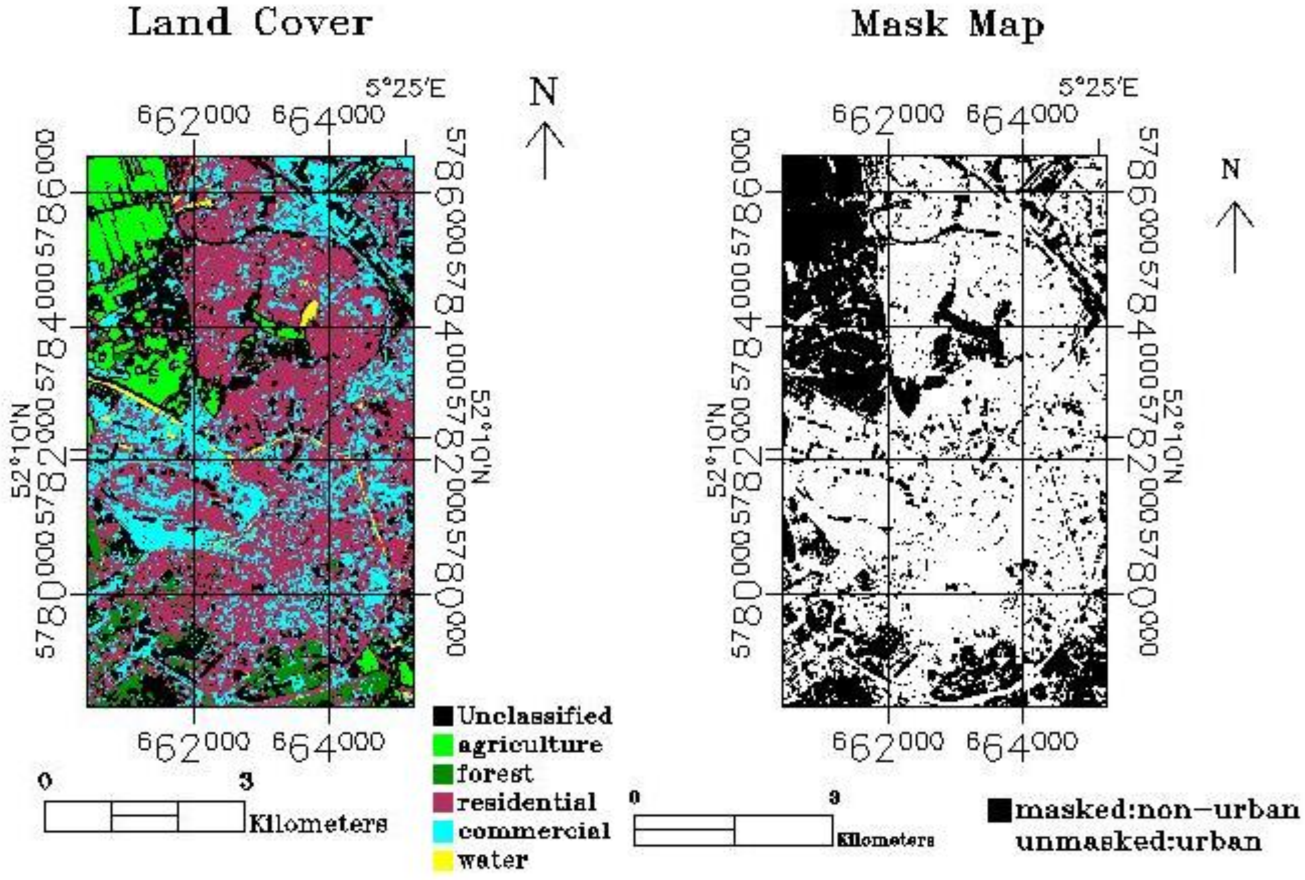

(A)

(B)

Figure 20 A map of supervised classification and a mask map for non-urban area. (A): Classification map, five classes were used: agriculture, forest, residential area, commercial area and water; (B): Mask map: Non-urban areas were masked.

The results of the Tasseled Cap transformation and the final impervious surface map are displayed in Figure 21. The non-urban area was masked so that the regression model was only applied to the urban area. The inner city (center part of image) and the new commercial area (north part) are almost completely identified as impervious surfaces. A main road goes through the forest and it was also identified as impervious, indicating that the obtained map is good. Overall, the impervious surface extraction by regression modeling gives a reasonable result visually.

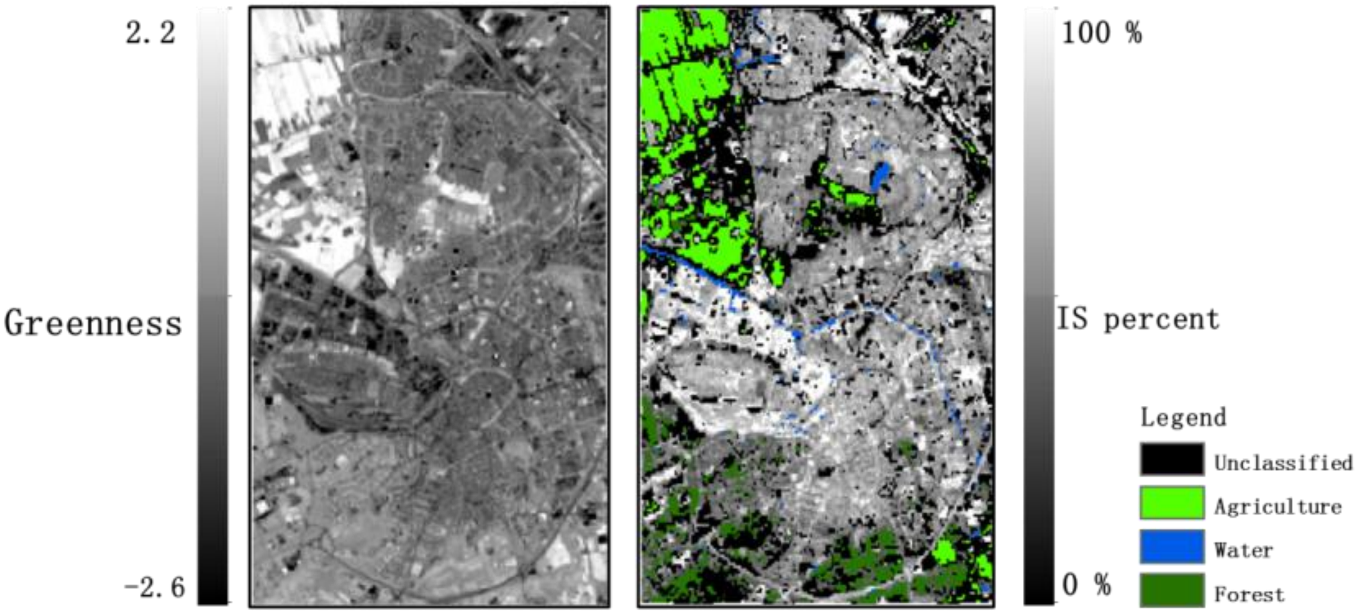

(A) (B)

Figure 21 Greenness and impervious surface map by regression modeling. (A): Greenness map; (B): Impervious surface map

The results of accuracy assessment are shown in the following. Figure 22-(A) illustrates the agreement between the estimated impervious (%) and the measured value. Ideally, all the sample points should be located on the diagonal line, and they are well-clustered around the diagonal line. It can be concluded that the agreement is high with a R^2 of **0.85**. In addition, the RMSE value was calculated as **14.79%**, indicating a promising agreement between estimated and measured imperviousness. Some systematic error (deviation from the axis) was observed by plotting residuals versus measured imperviousness, as shown in Figure 22-(B). For the area with a low impervious surfaces (less than 60% imperviousness), the regression model seems to be slightly overestimating, evidenced by many points existing above the residual line of zero. On the contrary, the model seems underestimate the impervious percent in the highly developed area.

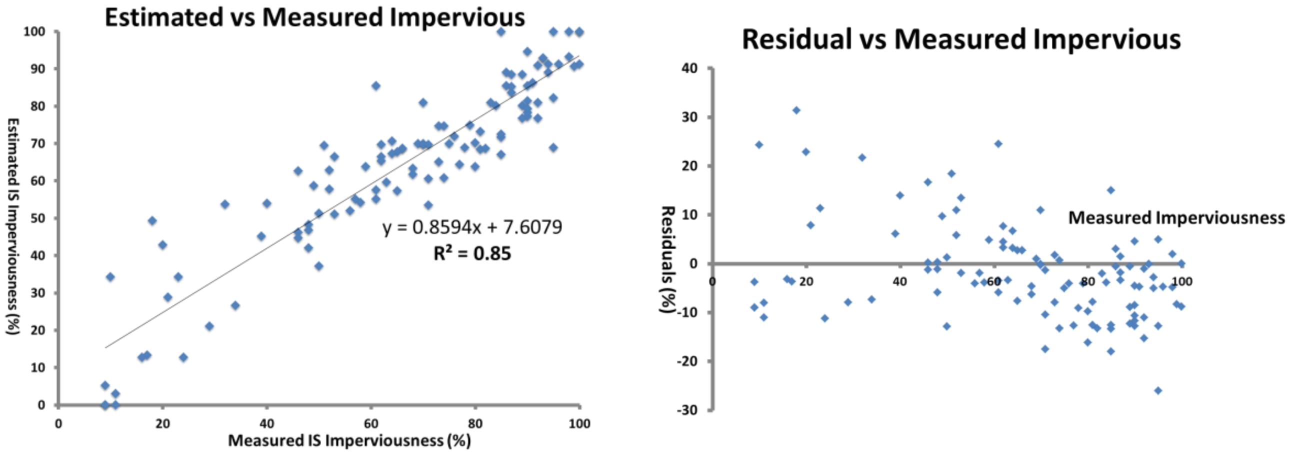

(A) (B)

Figure 22 Accuracy assessment for regression modeling method. (A): Plot between measured and estimated impervious surface percent; (B): Plot between measured impervious surface percent and residuals.

6.1.2 NLSMA approach with Landsat images

The NLSMA approach was performed five times with a series of Landsat images acquired in 1987, 1992, 1998, 2007 and 2014. Each time, three fraction images were produced. For reasons of space, examples of fraction images for only vegetation, soil and impervious surface in 2014 are given in this part (Figure 23) and the other fraction images are present in Appendix IV. From Figure 23, it can be seen that the distributions of vegetation, impervious surface and soil are well delineated. Vegetation is restricted to the agriculture area while impervious surface fraction is dominant in the inner city and its north part. Impervious surface is near zero in the agriculture and forest areas. Soil is mainly present in the southern part of the inner city.

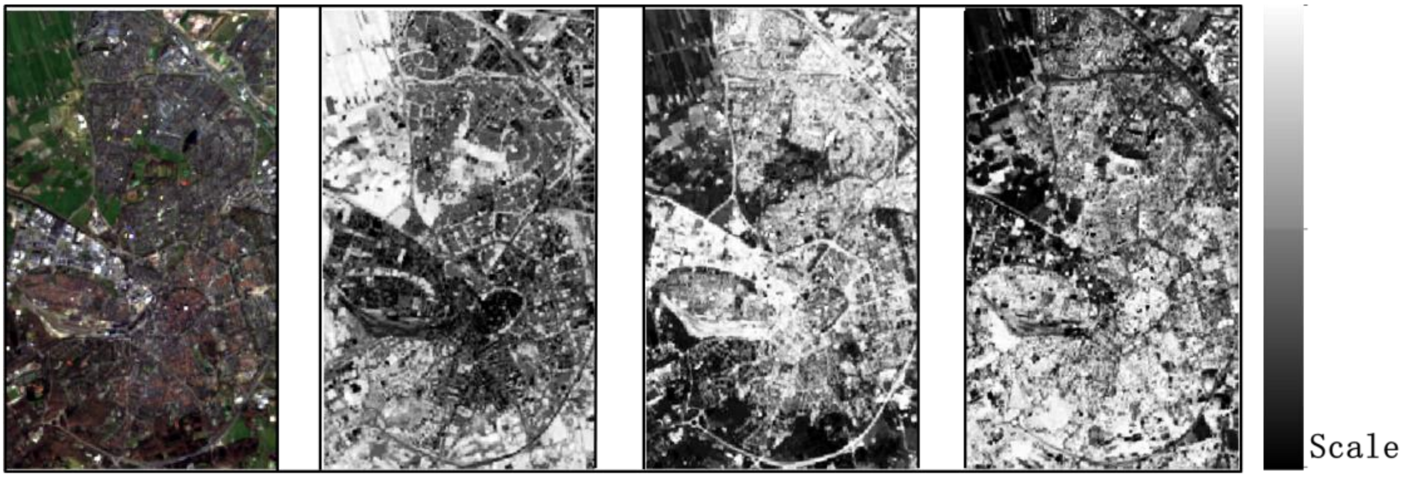

Figure 23 Fraction images of vegetation, impervious surface and soil mapped by NLSMA in 2014. (A): Landsat 8 image of study area; (B): Vegetation fraction; (C): Impervious surface fraction; (D): Soil fraction.

Similar to the accuracy assessment used for the regression model approach, a graph comparing the measured and estimated impervious surface fraction with 110 samples was generated (Figure 24). The agreement (indicated by R^2) between measured and estimated impervious surface fraction is as high as **0.89**. The residuals against measured impervious surface fractions were plotted as well. It can be seen that more residuals with values lower than zero were found, particularly for the developed area (%imp>50%). In addition, the RMSE and SE value for NLSMA were calculated as **9.38%** and **-4.20%**, respectively. A detail comparison and analysis of accuracy between the regression model and NLSMA approaches will be discussed in Chapter of Discussion.

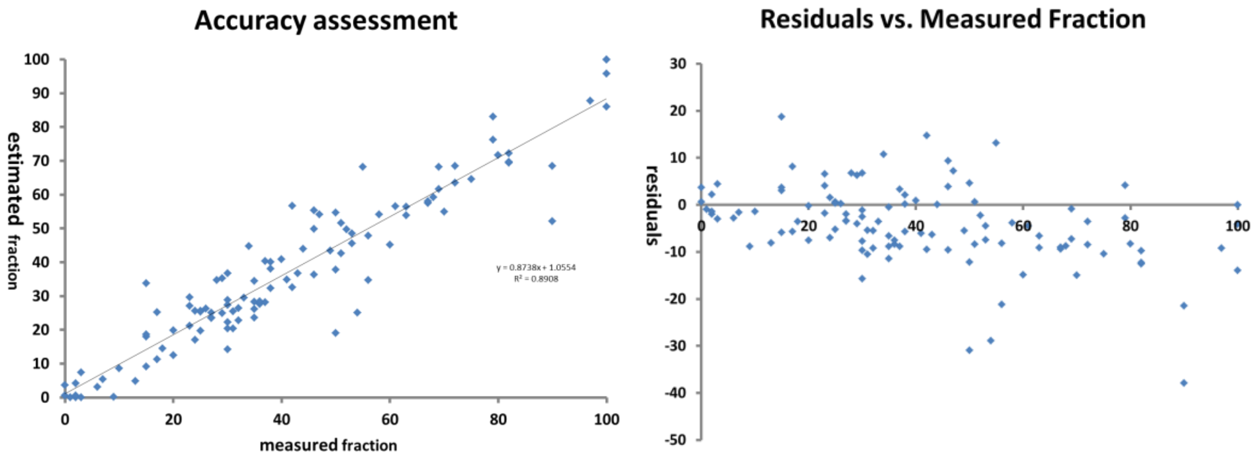

(A) (B)

Figure 24 Accuracy assessment for the NLSMA method. (A): Plot between measured and estimated impervious surface percent; (B): Plot between measured impervious surface percent and residuals.

6.1.3 Impervious surface changes

A series of impervious surface images of Amersfoort in 1987, 1992, 1998, 2007 and 2014 are shown in Figure 25. For a better visual comparison, the impervious surface fraction images were divided into four impervious surface levels as described in Table 12.

Development level	Criteria
None impervious surface	0 %<Imp <15%
Low impervious surface	15%<imp<30%
Medium impervious surface	30%<imp<60%
High impervious surface	60%<imp<100%

Table 12 Four land covers according to the impervious surface level.

In 1987, the impervious surface was only centered in the inner city with two main roads going through the rural regions. The northern part of the inner city was covered by vegetation and soil parcels. Five years later, the city grew significantly to its north, evidenced by the northern part of the inner city converting from non-impervious surface into medium or even high imperious surface level. It continued to grow to its north further and the new commercial and residential areas were almost completed by 1998. The urbanization process slowed down during the following ten years, evidenced by small differences between the impervious surface distributions of 1998 and 2007. In this ten-year period, the high-level impervious surface area reduced (indicated by decrease in red) compared to the situation in 1998. In addition, the agriculture area (upper left corner of each image) was recovered during this time frame, suggested by the conversion from low level to none impervious surface. A distinctive division between agriculture and urban areas is apparent in the north western part of the 2007 image. From 2007 to 2014, urbanization seems to expand outwards again, taking up the agriculture and forest areas. Some statistical summaries are given in the following.

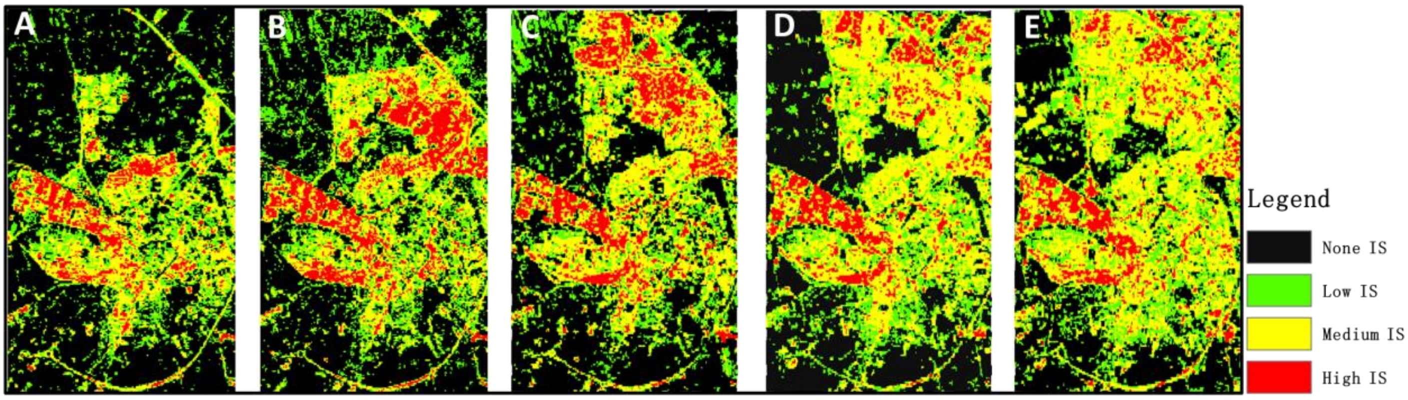

Figure 25 Impervious surface areas in Amersfoort. (A): 1987; (B): 1992; (C): 1998; (D): 2007; (E):2014;

Statistical summaries of the urbanization process are shown in Figure 26 and Table 13. Table 13 gives an original statistical description and Figure 26 gives a clear view about how the impervious surface changed in the last 27 years according to different impervious surface levels. It can be seen that from 1987 to 2014, impervious surfaces in the study area have continually increased for during the last 27 years. In 1987, only **15.87 km^2** (**40.75%** of total area) was covered by impervious surface and this number has increased to **27.01 km^2** in 2014, a **70.20%** increase in impervious surface area in these 27 years. The periods from 1987 to 1998 and from 2007 to 2014 experienced a fast urbanization process with **13.73%** and **7.84%** increase in impervious surface, respectively. It can be concluded that most of the impervious surface area was covered by medium impervious surface. The medium impervious surface increased dramatically from **7.68 km^2** (19.72% of total area) in 1987 to **15.69km^2** (40.28%) in 2014. The high-level impervious surface area remained at approximately **3 km^2** (7%), except for a rapid increase from 1987 to 1992 (from 1.27 km^2 to 3.43 km^2). The low-level impervious surface was maintained at **7 km^2** throughout the 27 years.

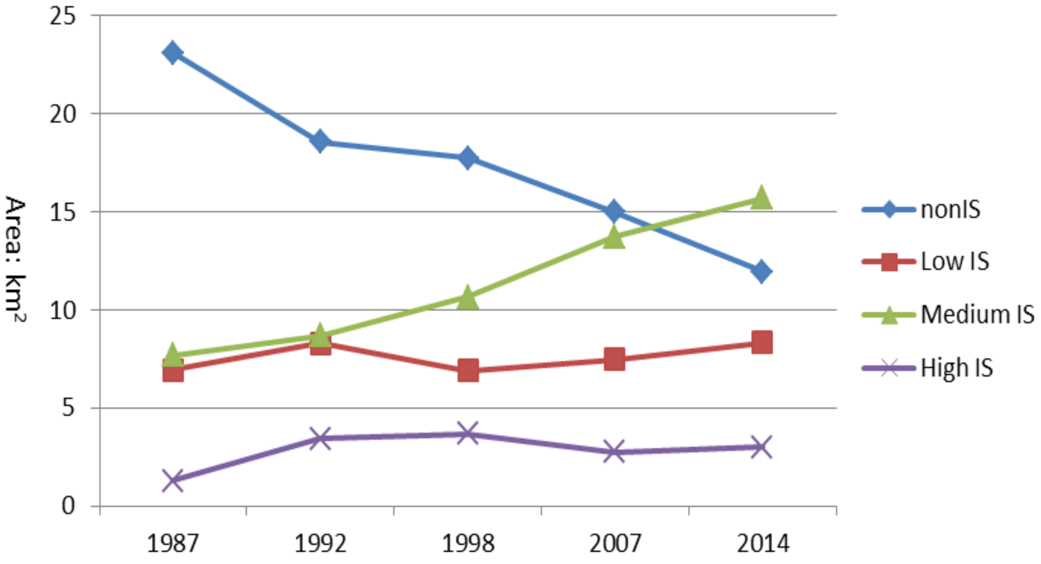

Figure 26 The changes of impervious surface areas from 1987 to 2014

Total area of study area: **38.95km^2**							
Year	**Non IS in km2**	**Non IS in**	**IS in km2**	**IS in percent**	**Detailed impervious surface category analysis**		
1987	23.08	*59.25%*	15.87	*40.75%*	Low IS (km^2/ %)	6.92	*17.76%*
					Medium IS (km^2/ %)	7.68	*19.72%*
					High IS (km^2/ %)	1.27	*3.27%*
1992	18.55	*47.63%*	20.4	*52.37%*	Low IS (km^2/ %)	8.29	*21.28%*
					Medium IS (km^2/ %)	8.68	*22.28%*
					High IS (km^2/ %)	3.43	*8.81%*
1998	17.73	*45.52%*	21.22	*54.48%*	Low IS (km^2/ %)	6.91	*17.74%*
					Medium IS (km^2/ %)	10.64	*27.32%*
					High IS (km^2/ %)	3.67	*9.42%*
2007	14.99	*38.49%*	23.96	*61.51%*	Low IS (km^2/ %)	7.46	*19.15%*
					Medium IS (km^2/%)	13.74	*35.27%*
					High IS (km^2/ %)	2.76	*7.09%*
2014	11.94	*30.65%*	27.01	*69.35%*	Low IS (km^2/ %)	8.32	*21.36%*
					Medium IS (km^2/ %)	15.69	*40.28%*
					High IS (km^2/ %)	3	*7.71%*

Table 13 Statistical summary of the impervious surface areas for Amersfoort in 1987, 1992, 1998, 2007 and 2014.

6.1.4 DTC mapping approach with FORMOSAT-2 image

Figure 27 shows the result of DTC with four test images. The DTC result for the whole study area can is presented in Appendix V. In our results, the land covers types of soil and vegetation were grouped into a single land cover: previous surface. In Figure 27, the geometry and location of impervious surfaces such as roads, bridges and buildings are clearly delineated. A visual comparison suggests that DTC serves as a good tool for impervious surface extraction using high resolution images.

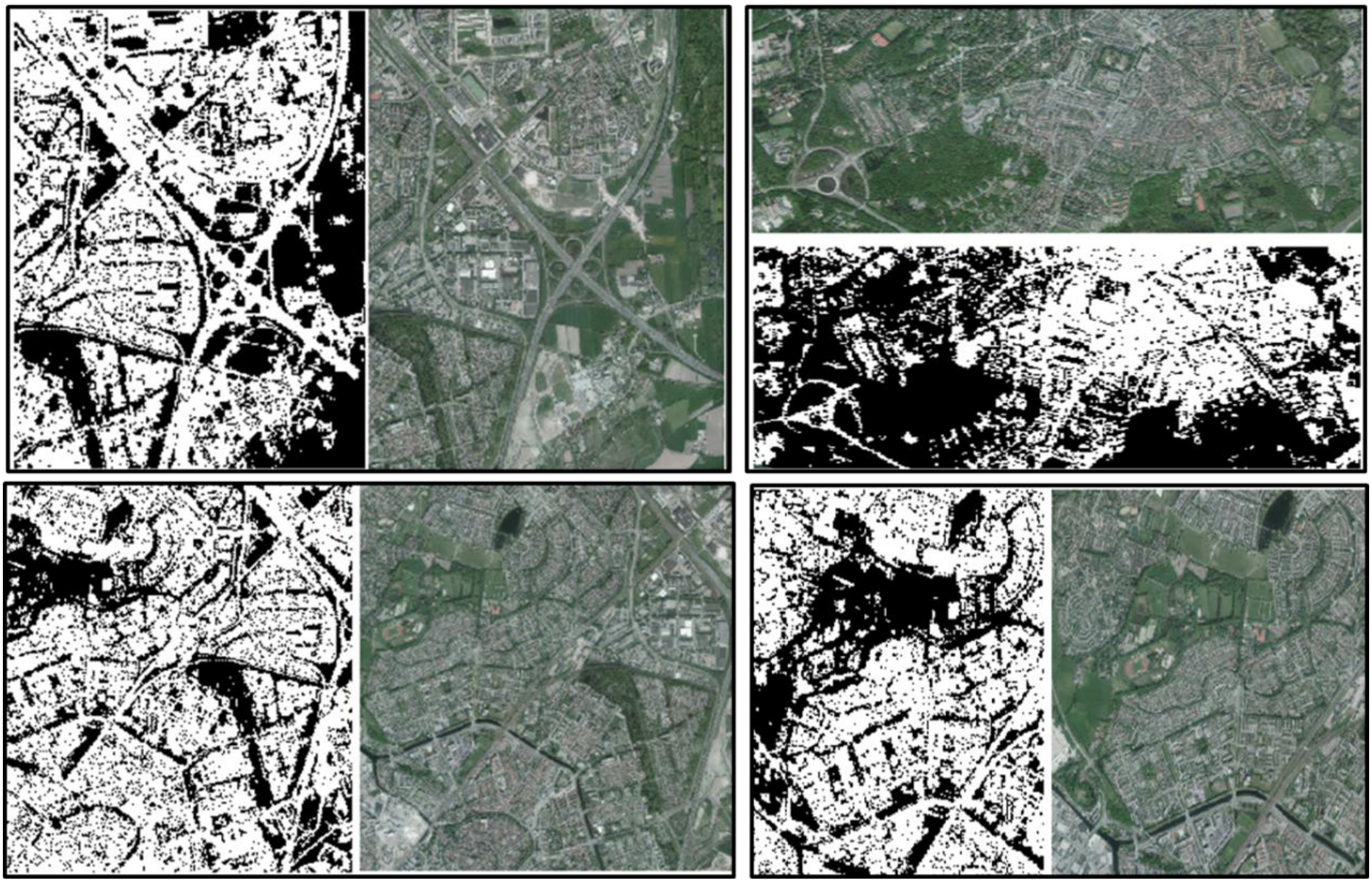

Figure 27 Impervious surface areas mapped by DTC at four test sites (The impervious surface areas mapped by DTC are shown on the left, the IPO Luchtfoto actueel of Amersfoort is shown on the right).

Source: IPO Luchtfoto actueel of Amersfoort, 2011

The error matrix is given in Table 14. 340 impervious surface pixels and 352 pervious surface pixels were collected based on the impervious surface map. Impervious surface had a producer's accuracy of **92.28%** and a user's accuracy of **91.47%**, respectively. These two numbers were **91.83%** and **92.61%** for non-impervious surfaces. The overall accuracy and KAPPA value were up to **92.05%** and **84.10%** respectively, suggesting that the DTC approach performed perfectly according to Landies and Koch's (1977) agreement measures in the impervious surface extraction in urban scale.

	Impervious surface	**None impervious surface**	**Row total**	**User's accuracy**
Impervious surface	311	29	340	91.47%
None impervious surface	26	326	352	92.61%
Column total	337	355	637	
Producer's accuracy	92.28%	91.83%		
Overall accuracy: **92.05%**; KAPPA: **84.10%**				

Table 14 Error Matrix for DTC

6.2 Runoff modeling analysis

6.2.1 Runoff increase with impervious surface changes

The extent of the runoff after the storm that occurred on June 3, 2008 is given in Figure 28. The white dots in the images are representing buildings and were excluded. Overall, more runoff responses and a higher volume of runoff are expected in 2014 visually compared to the result of 1987. The eastern part of the study area is almost completely free of runoff in 1987 due to the lower level of imperviousness at that time. The situation is worse in 2014, more pervious surfaces having been converted to impervious surfaces.

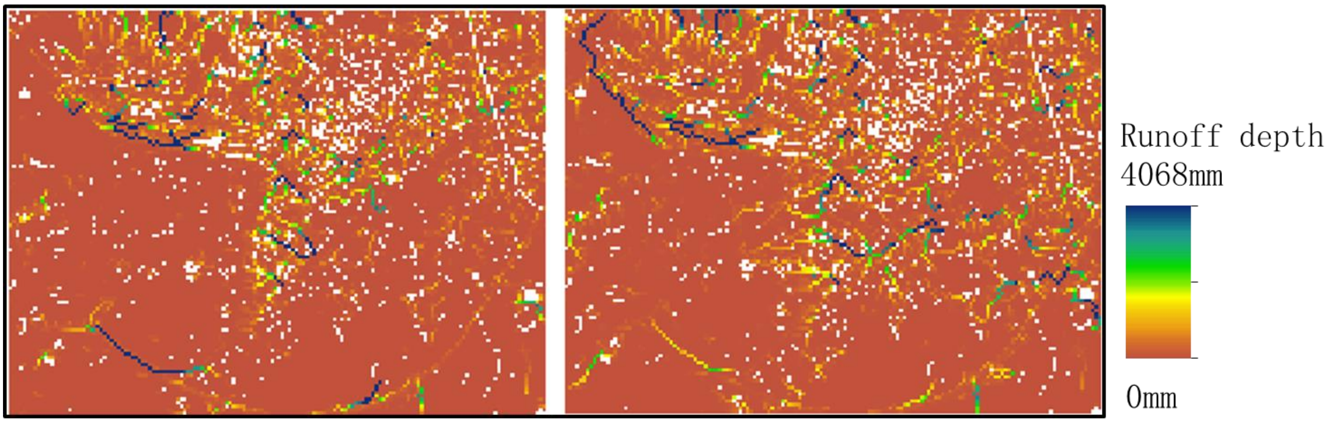

(A) (B)

Figure 28 Spatial runoff patterns and depth for a storm case of June 3, 2008. (A): Year of 1987; (B): Year of 2014

Figure 29 shows a comparison of the runoff depth distribution in 1987 and 2014. Most of the area has a runoff depth lower than 30mm. The total area with a runoff depth below 30 mm was **13.43 km^2** in 1987 and **12.62 km^2** in 2014. We consider a runoff depth of **200 mm** as a warning threshold, which means that, if the runoff depth exceeds 200mm, then these areas are in danger of being inundated and relatively severe damage to the infrastructure of these areas may be expected. The inundated area is around **0.29 km^2** for 1987 while it rises to **0.51 km^2** for 2014. A significant increase of **80%** is observed as the result of the expansion of impervious surface in these 27 years.

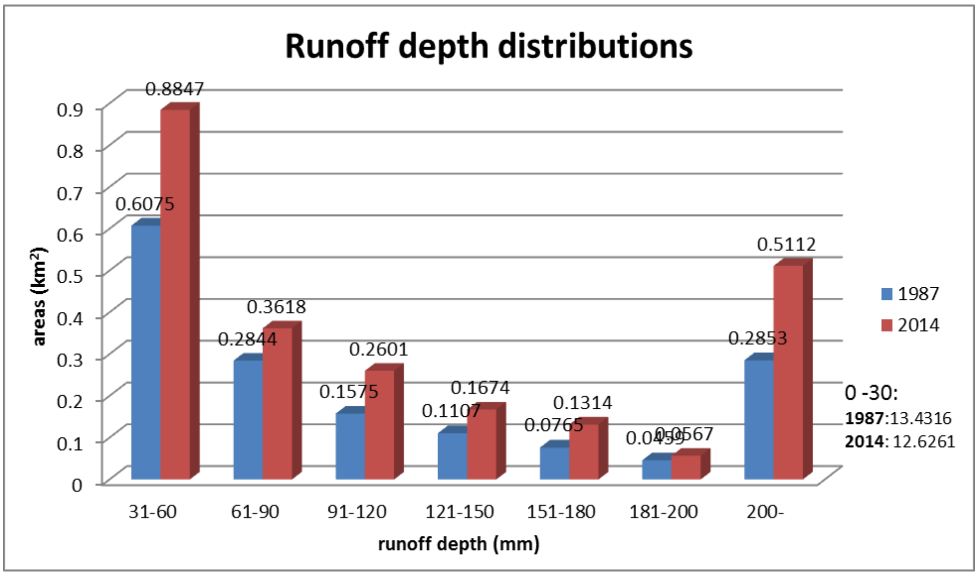

Figure 29 Simulated runoff depth for the cases of 1987 and 2014

The most vulnerable places are located at the upper left corner of the study area, where the Amersfoort railway station is located (marked by the yellow star in the image below). Figure 30-(A) shows an overview of the landscape around the Amersfoort central station and the railway is delineated by black lines. These extreme depths, indicated by a blue and yellow circle in Figure 30, are present around 0.9 km to the west of the Amersfoort central station (labeled by a yellow information mark). The water flow runs from west to east, as indicated by the blue arrow in Figure 30-(B), -(C). The extreme runoff depth was simulated as high as around 4000 mm. The situation has become exacerbated since then because, for 2014, another runoff flow within the railway was observed 1.5 km to the west of the railway station, as shown in a yellow circle. This water flow originates at the edge of railway and flows along the railway to the northwest and, furthermore, goes through a residential area, as indicated by the yellow circle and arrow in Figure 30-(C). The average runoff depth was simulated around 1900mm in this region, which is, of course, a deadly situation. Therefore, the Amersfoort central station and the residential area to its north direction are the most vulnerable places for a flood in a case of intensive rainfall.

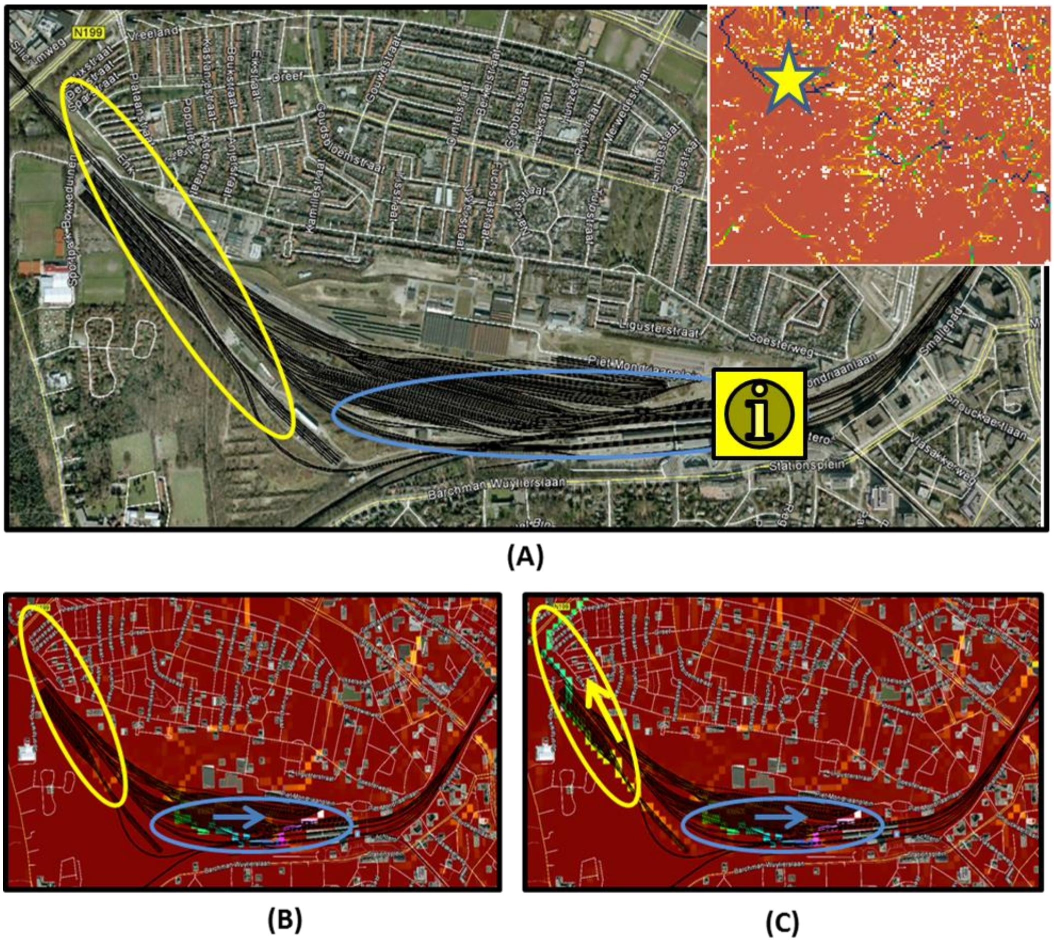

(A)

(B)

(C)

Figure 30 Overview and the runoff patterns at Amersfoort central station for two cases of 1987 and 2014. (A): An overview of the Amersfoort central station; (B): The runoff pattern at central station in 1987; (C): The runoff pattern at central station in 2014.

Source: Google Earth, (2005). Amersfoort central station, 51°06'24.27"N, 5°25'28.40"W. elevation 4310m. 3D buildings data layer. [Viewed 3rd December 2014].

6.2.2 Runoff spatial patterns

The runoff spatial patterns at high spatial resolution are presented in the following.

The original runoffs were raster maps representing the runoff depth on the ground. Considering that a runoff on the street with a depth larger than 300 mm has the potential to flood into buildings and infrastructure, therefore a threatening threshold of **300 mm** was selected so that only the runoff exceeding the 300 mm depth was remained. For a better visual presentation, the runoff flows were converted to the runoff vector features, as indicated by the black lines in Figure 31. By examining the properties of runoff flows, a large number of small runoff fractions only five or ten meters in length were found. Taking into account that the small runoff fractions are far less significant than the major runoff flows, only the runoff flows with lengths of more than 50 meters were retained. This post-model processing is shown in Figure 31.

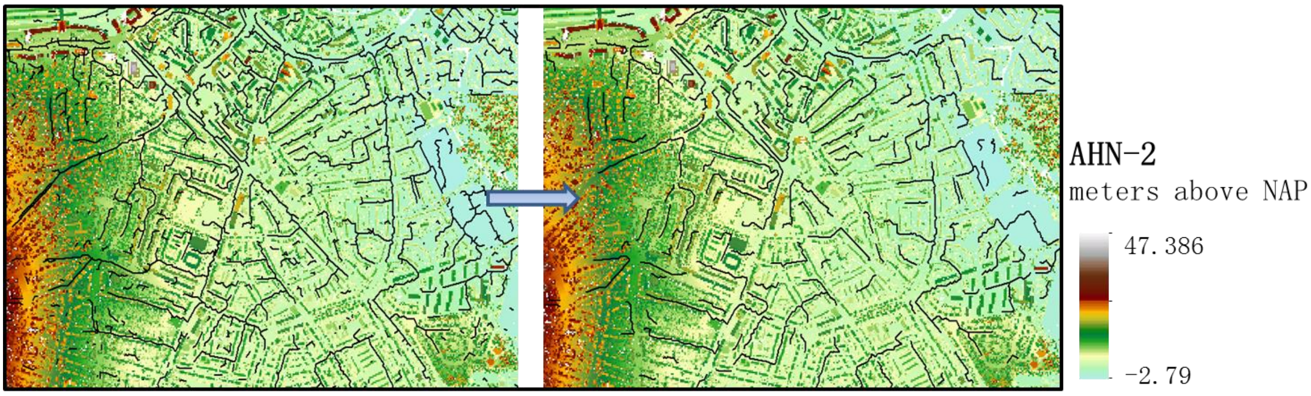

Figure 31 Post-model runoff processing. (A): Original runoff flows; (B): Runoff flows after post-model processing.

DEM source layer: AHN-2, 2012

An inspection of the runoff spatial distribution was performed by examining the runoff pattern in Google Earth (2014). Two testing sites (Figure 32) were selected as examples to illustrate the fitting between locations of runoff flows and actual landscapes. It can be concluded that the extents and locations of simulated runoff match the urban streets very well. Therefore, the spatial patterns produced by the runoff model were reliable for further analysis.

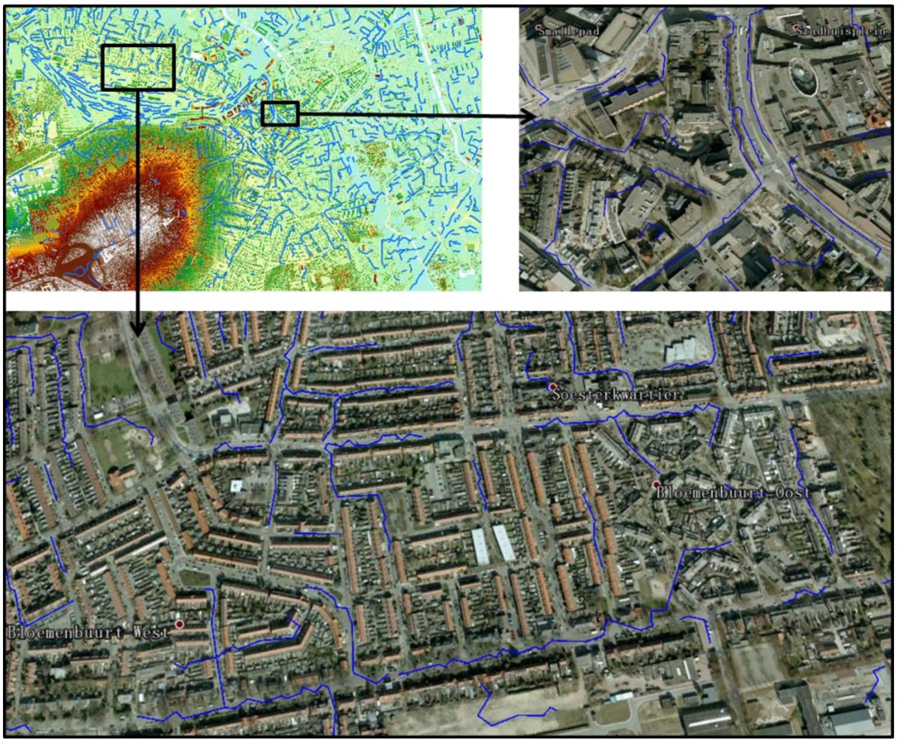

Figure 32 Examination of simulated runoff with the streets at two testing sites.

Source: Google Earth, (2005). Amersfoort, elevation 2300m. 3D buildings data layer. [Viewed 3rd December 2014].

6.2.3 Comparing spatial patterns of potential damaging runoff

The potential damaging runoff flows for various rainfall intensities and recurrence frequencies are shown in Figure 33. The four sub-figures, (A), (B), (C), and (D), illustrate the spatial patterns of runoff for storms of 10, 14, 18 and 23 mm/hour that can be expected every half-year, one year, two years, and five years, respectively. It can be seen that the runoff response of a storm of 23mm/hour is overwhelming and it seems that some urban infrastructures are vulnerable for inundation. On the other hand, a storm of 10 mm/hour is not a threat to most regions in Amersfoort except for the railway station, where some runoff flows were still present. In addition, runoff flows seems to be significant around the edge of the higher elevated hill. A reasonable explanation is that the steep slopes in the hilly region accelerate the runoff processes and may further boost the accumulation of runoff when entering the urban area downstream.

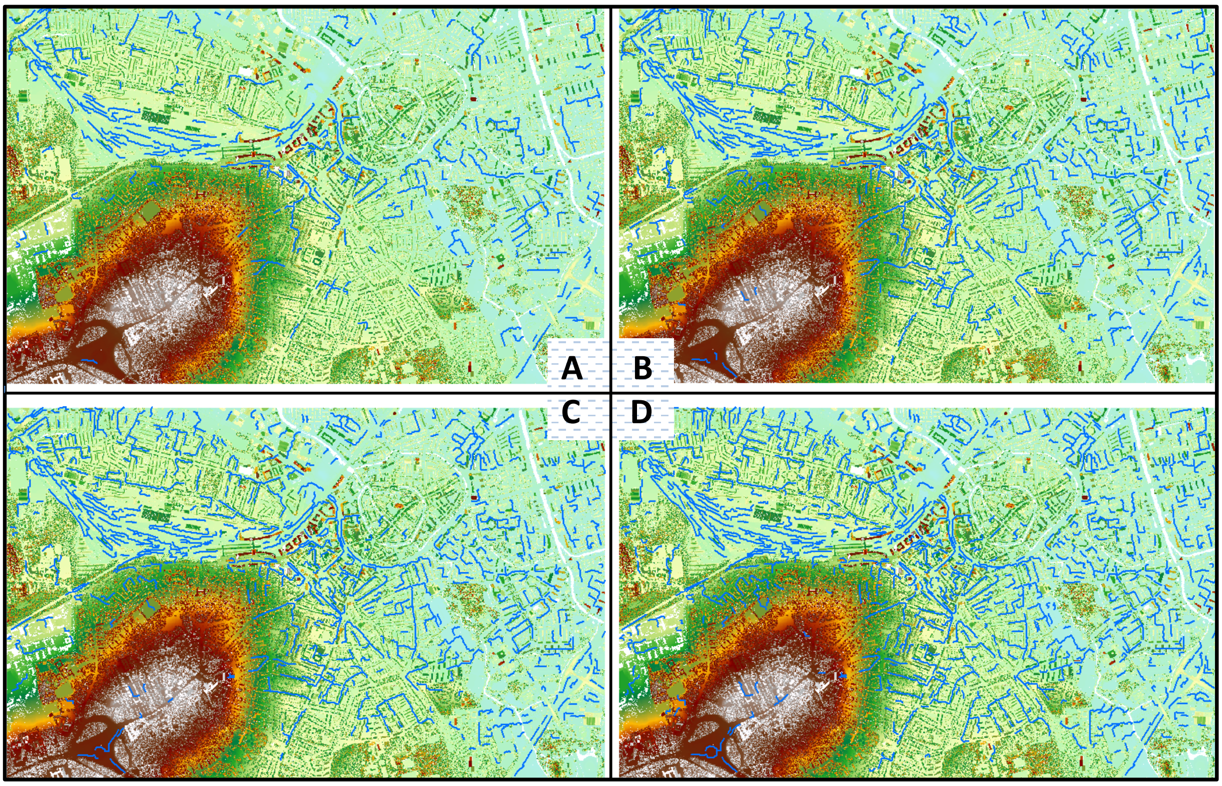

Figure 33 The dangerous runoff flows for various rainfall intensities. (A) Spatial runoff patterns for a rainfall event of 10 mm/hour; (B): Spatial runoff patterns for a rainfall event of 14 mm/hour; (C): Spatial runoff patterns for a rainfall event of 18 mm/hour; (D): Spatial runoff patterns for a rainfall event of 23 mm/hour.

DEM source layer: AHN-2, 2012

6.2.4 Urban runoff risk mapping - buildings

Nearly 32,000 parcels in the study area were labeled by risk level, according to the threat criteria that described in the section of risk maps for buildings. Figure 34 shows an enlargement of the region delineating the buildings of various risk levels for a rainfall of 23 mm/hour. Figure 35 illustrates the risk map of buildings for a one-hour rainfall event of 23 mm/hour. These illustrations are intended for use by the government in assessing the risks presented by moderate to severe rainfall intensities. The buildings that are located beside the streets with runoff flows are at a relatively high level of risk. It can efficiently direct the city managers to distribute the relief resources reasonably. The risk maps of buildings for the other rainfall intensities are listed in Appendix VIII.

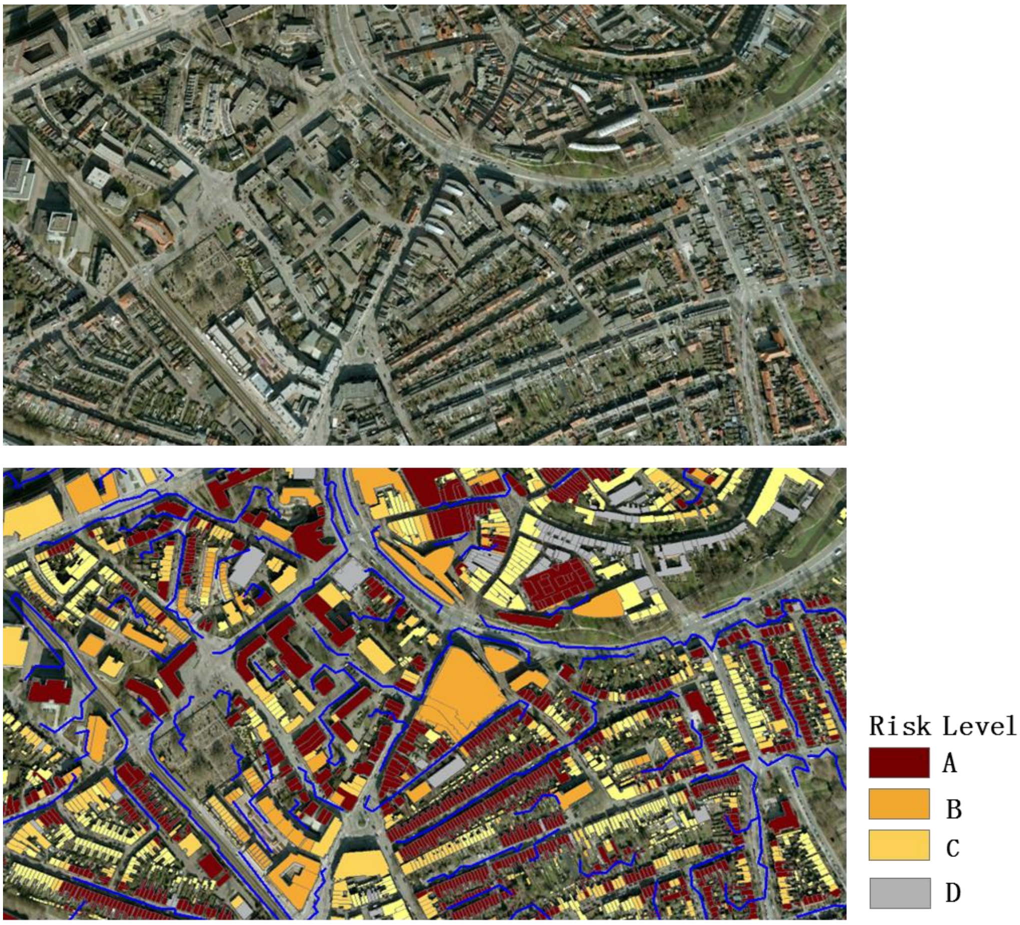

Figure 34 The risk map for buildings in a case of 23 mm/hour storm.

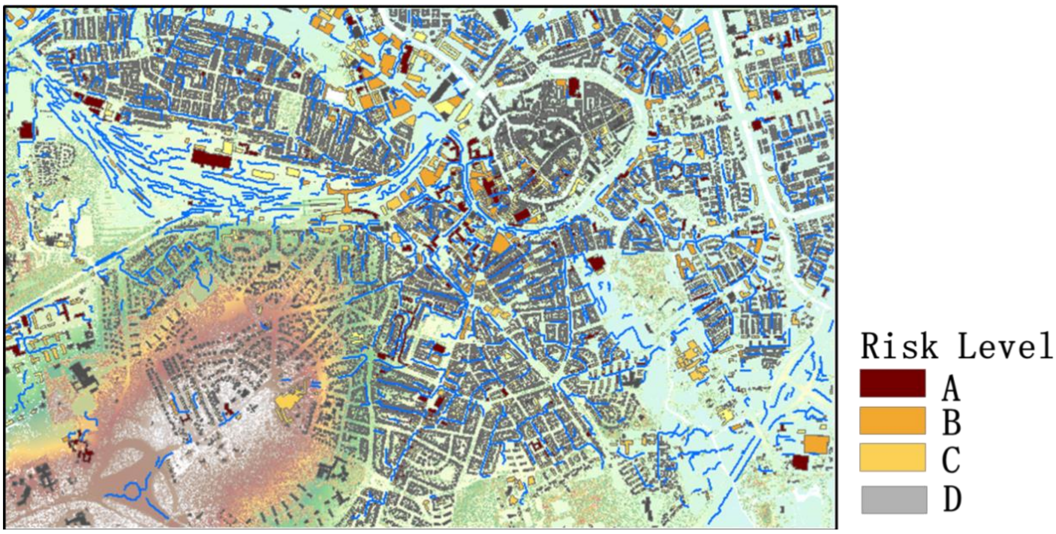

Figure 35 The distribution of risk buildings for a rainfall event of 23 mm/hour.

7. Discussions

The uncertainties observed in the mapping results and the advantage and constraints for various mapping methods are discussed. In addition, discussions about the performance of the runoff model and the results of runoff modeling are presented.

7.1 Impervious surface mapping

7.1.1 Uncertainties for regression modeling

Our results were compared to results of previous research by Bauer et al. (2004). They used the regression modeling approach to map impervious surfaces for the state of Minnesota in 1990 and 2000. They obtained an overall R^2 value of 0.86 and standard error of 11.8 and 11.7. This research had an overall accuracy of 0.85, which is very promising and comparable to Bauer's results.

Some uncertainties were observed in the images and the possible reasons are explained here. One of the uncertainties is the confusion between the bare soil and impervious surface areas. Bare soil was determined to be land cover with a low greenness by tasseled cap transformation. Therefore it was identified as impervious surface by regression modeling. However, this is not necessarily true. An example of this uncertainty is shown in Figure 36. The center of the left image shows that the middle is occupied by bare soil. However, in the impervious surface percentage map on the right, it was recognized as a completely impervious surface.

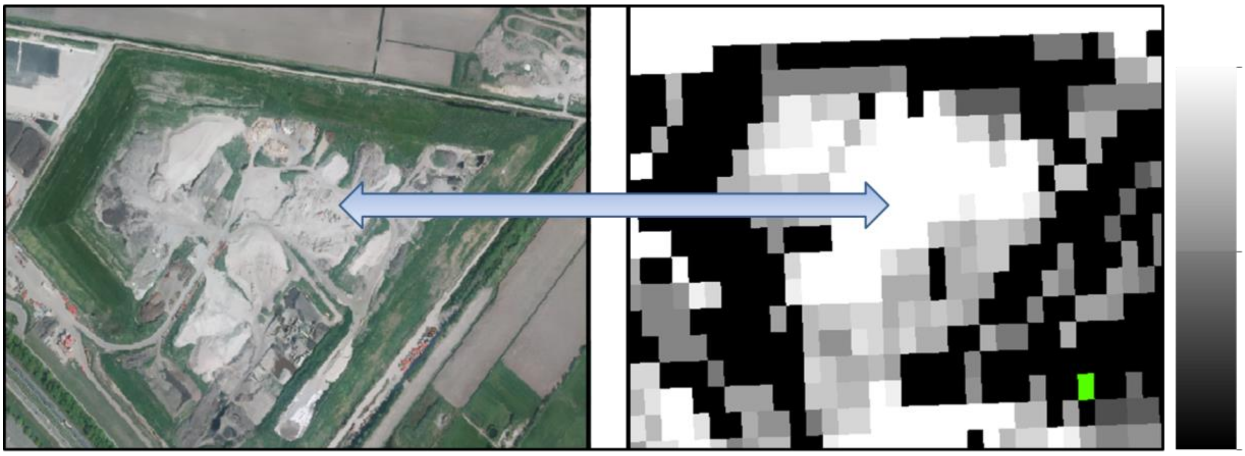

Figure 36 Bare soil classified as an impervious surface. IPO Luchtfoto actueel (2011) is on the left and the impervious surface percentage map is on the right.

Another uncertainty is caused by misclassifications of urban and non-urban areas. This uncertainty is usually seen at the boundary between urban and non-urban areas. If a pixel at this boundary is classified as a non-urban area, then it will not be taken into account for further impervious surface mapping. The last uncertainty is that some water was recognized as an impervious surface by regression modeling. This class confusion can be removed by masking the water body by digitization.

7.1.2 Uncertainties for NLSMA

The main uncertainties associated with NLSMA approach is discussed in the following. It is associated with the shade effect caused by topology and buildings in urban area. Figure 37 shows three spectrums of pure impervious surface, pure soil and impervious surface with shade. The spectral shape and features of the pure impervious surface and the pure soil are completely different. The spectrum of impervious surface with shade is more similar to the spectrum of the pure soil due to a reduction in brightness in band 1 to 3 and an increase in brightness in band 4 to 6 that is caused by shade. Therefore, the NLSMA mapper may classify some part of these areas as soil, rather than impervious surface in shade. As a result, the soil fraction tends to be overestimated, while the impervious surface fraction is underestimated where shade is present. This shade effect can explain the underestimation in impervious surface in developed areas. As in commercial and residential regions, intensive shade is common due to the tall buildings. Therefore, the impervious surface fraction in the developed area was likely underestimated in our results.

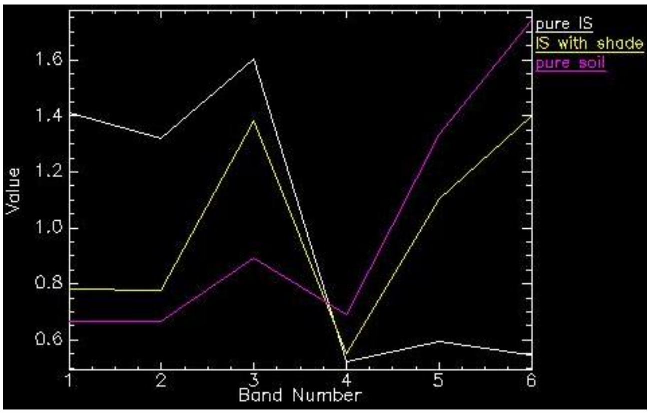

Figure 37 An example of the shade effect in residential area. The impervious surface fraction calculated by NLSMA (left rectangle) is only 55%, while the actual fraction is measured as high as 70% (right rectangle).

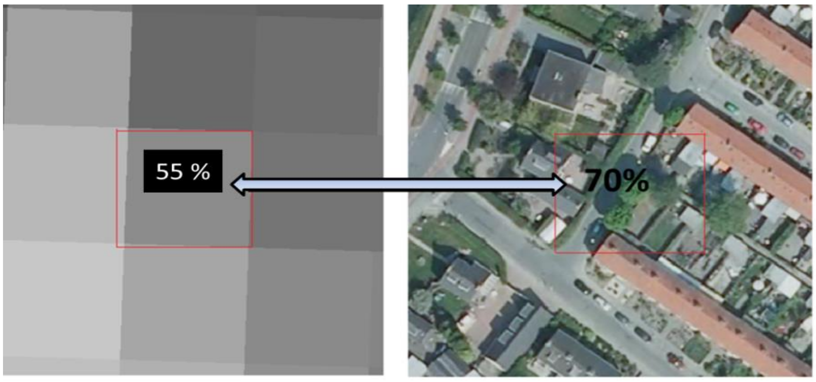

Figure 38 Underestimation in impervious surface areas due to the shade effect. Impervious surface (%) is shown on the left, a zoomed-in view of IPO Luchtfoto actueel (2011) is illustrated on the right.

7.1.3 Uncertainties for DTC

Our DTC results are comparable to previous research. Lu and Weng (2009) extracted impervious surface area using IKONOS images using the DTC approach and with an overall accuracy of 92%. Goetz et al. (2003) mapped the impervious surface with IKONOS imagery by DTC and obtained an overall accuracy around 90%. The impervious surface extraction in Amersfoort in this study obtained similar results with an accuracy of **92.05%** with a KAPPA index: **84.10%**. This indicates that the DTC approach is very promising and can be widely-used for impervious surface mapping in urban areas.

Although the result is very accurate, there is still some misclassification that is mainly related to uncertainty in the thresholding. Ideally, a threshold ranging from 0.95 to 2.50 can be used to separate soil from impervious surface. However, if the threshold is set close to 2.50, the soil fraction would decrease greatly and only a small part of the soil fraction will be mapped. So an overestimation of impervious surface can be expected. On the other hand, if the threshold is set close to 0.95, then the result is dominated by the soil fraction. Figure 39 illustrates a comparison of a test site image using different soil thresholds. It is clear that a small threshold results in a severe salt-and-pepper effect in the impervious surface classification, which hampers the accuracy. Through several tests, a threshold of 2.0 was accepted because it gave the best performance for impervious surface separation.

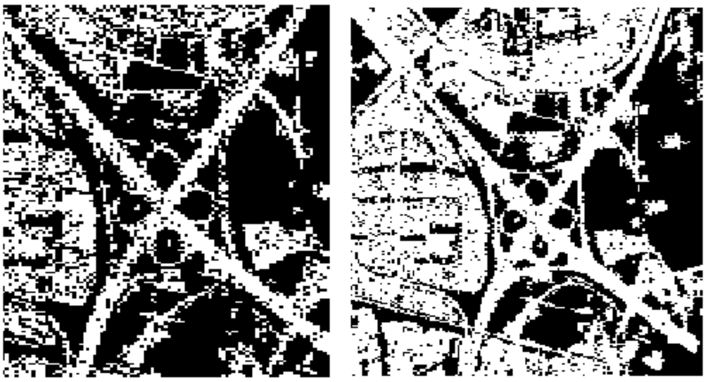

(A) (B)

Figure 39 Comparisons between impervious areas map with a different threshold to separate soil and impervious surfaces. (A): Soil threshold-1.0; (B): Soil threshold-2.0;

7.1.4 Comparing regression modeling and NLSMA

For a detail analysis and comparison between NLSMA and regression modeling approaches, the study area was divided into two categories: less developed areas with less than 50% impervious surface, and developed areas with more than 50% impervious surface (Table 15). Two accuracy indexes, RMSE and SE were used to analyze and compare their performance. A low overall RMSE value (**9.38%**) for NLSMA indicates that it performed better than the regression modeling approach for the whole study area. Detailed analysis shows that both approaches perform better in less developed areas than in developed areas. However, the SE values indicate that a slight underestimation is observed in the

NLSMA approach, while regression modeling is less biased. The underestimation in NLSMA is more significant in developed areas (**-8.54%**) than in less developed areas (**-2.09%**).

Accuracy assessment		**NLSMA (%)**	**Regression Modeling (%)**
RMSE	Overall	9.38	14.79
	Less Developed	7.52	12.94
	Developed	12.34	15.30
SE	Overall	-4.20	-0.27
	Less Developed	-2.09	3.09
	Developed	-8.54	-1.26

Table 15 A detail comparison between NLSMA and regression modeling. Less developed areas: <50% imp; Developed areas: >50% imp.

7.1.5 Advantages and constraints

The advantages and constraints for each impervious surface mapping method need to be specified.

Although the regression modeling approach has the lowest accuracy in the results, it is still widely used as it is appropriate for impervious surface mapping at a large scale, such as an area of a province or a state. For a large scale mapping, the non-urban area will be blocked by a mask map and the regression model is only applied to the urban area. By doing this, the impervious surface map within the urban area combined with a general overview of the distribution of land covers outsides the urban area can be generated. This is the most efficient way to map impervious surface in a large scale. One of the major constrains for regression modeling approach is that it dismisses the component of bare soil when map the impervious surface, which will leads to some significant uncertainties. These uncertainties may be dramatic when a large scale of urban area is under construction. Another constraint is its relative low efficiency compared with NLSMA approach. For every mapping area (each image), an independent regression modeling should be constructed for an unbiased result. However, the development of regression modeling is normally done by manual digitizing, which cost quite a lot of time and human effort.

NLSMA is a promising approach for impervious surface mapping on the basis of satellite images with a medium spatial resolution. It has a higher accuracy than the regression modeling approach and is much more efficient as it make full use of the automatic mapper that is available in image process software. NLSMA is appropriate for monitoring the impervious surface changes at a local urban area because the spatial patterns of impervious surface, vegetation and soil can be mapped with high accuracy. The shortcoming for NLSMA approach is that the highly developed area is always underestimated due to the shade caused by buildings and topography.

The highest accuracy was achieved by the DTC approach that deals with images with a high spatial resolution. Detail impervious surface map produced by DTC is more appropriate for further quantitative studies such as urban flash flooding. On the other hand, DTC is not applicable for a large scale mapping due to the large amount of satellite data at a high spatial resolution.

7.2 Runoff analysis

7.2.1 Performance of runoff model

Some limitations of this model are apparent and need to be specified. One of the problems is the overestimation of runoff depth. The deepest runoff always occurs at the Amersfoort central station with a height of up to several meters. This is far beyond the runoff generated in reality. The significant overestimation can be explained by the simplified runoff drain network used in the model. A local drain direction (LDD) was calculated from the DEM. For each grid cell, the LDD map determines the direction in which the water will flow by calculating the steepest slope. In this case all the rainfall upstream will contribute to the runoff accumulation downstream without any dispersion. This will result in a high runoff depth downstream (Figure 40-(A)). In reality, a part of the runoff water will disperse during the runoff acceleration and the runoff in the downstream area is not that high (Figure 40-(B)).

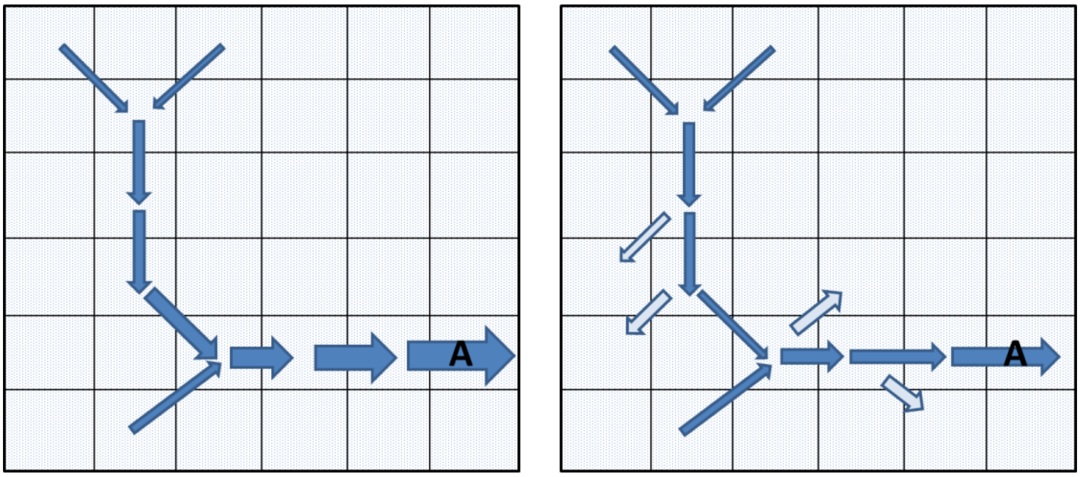

(A) (B)

Figure 40 Runoff process in model and in reality. (A): Runoff process in the model; (B): Real runoff process.

Another limitation associated with this model is that the urban sewage system is not included. A drainage system is the most effective way of reducing the impact of runoff in urban areas. Adding the local drainage system to the runoff model is likely to increase the accuracy of the model. However, it was not integrated as it was outside the scope of this study and not easy to implement.

7.2.2 Runoff spatial patterns and risk maps of buildings

Spatial patterns of runoff in urban areas are the basis for decisions by the urban water conservancy department and other government departments that deal with water. They give a clear overview of the extent and location of major runoff. An urban flooding risk map for buildings can be further mapped when it is associated with infrastructures properties. Risk maps are very valuable in guiding the urban construction department to optimize the urban drainage system, in helping government decide whether and where to take actions to protect vulnerable infrastructure when a rainfall or high water event is coming. In addition, if the model can be combined with a weather forecast system, an early warning urban flooding forecast system can be built.

7.2.3 Remarks for Amersfoort

Based on the runoff analysis in this thesis, regions next to a hillside have a higher risk of urban flooding than the inner city. More attention should be paid to these regions, especially to the central station when a storm with a return time of more than 2 years is expected. The location of Amersfoort central station is poorly chosen. It is located right beside the only hill in the area, making it vulnerable to several natural hazards such as flooding.

8. Conclusions

Various approaches have been developed for impervious surface mapping using different types of satellite data. The specific approach depends largely on the remote sensing data available. In this thesis, impervious surface mapping approaches with both medium and high spatial resolution were investigated. A series of 5 Landsat images of Amersfoort acquired between 1987 and 2014 were used and the regression modeling and NLSMA approaches were applied. Both methods mapped impervious surface in Amersfoort successfully. Regression modeling achieved an accuracy of **85%,** which indicates it has a high agreement with the real landscapes. NLSMA performed better, obtaining an agreement of **89%**. Another two statistical measures - RMSE and SE, were calculated for a detail comparison between them. Overall, NLSMA performed better, evidenced by a lower RMSE (9.38%) compared to the regression modeling (14.79%). However, in the built-up area, slight underestimation was observed mainly due to the shade effect while the regression modeling seems less biased for the entire urban area.

Some advantages and constraints for the regression modeling and NLSMA are pointed out here. Although regression modeling had the lowest accuracy in the result, it is more appropriate for large scale impervious surface mapping (such as a state or a province) because that the regression model is only applied to the urban area while the areas outside the urban area are masked by the land covers classifications. The results of regression modeling not only show the distribution of impervious areas within the urban area, but also illustrate the distribution of land covers outside the urban area. Regression modeling has a requirement of satellite images that it should be acquired on a leaf-on season for a reliable result. NLSMA approach is sufficient and appropriate for impervious surface changes mapping. It makes full use of automatic mapper which can improve the efficiency significantly. NLSMA can delineate impervious areas as well as the soil and vegetation distribution. It should be noted that the shade effect causes slight underestimations, especially for the highly-developed areas.

Apart from mapping impervious surfaces with medium spatial resolution images, another DTC approach was used to map the impervious areas with a FORMOSAT-2 image acquired in 2013. DTC achieved an overall accuracy of **92.05%** with a KAPPA value of **84.10%**, proving that it is a very promising approach in impervious surface mapping. The result of DTC can be used for furthermore quantitative study such as urban (flash) flooding because the impervious area can be mapped in a great detail and with a high accuracy. However, due to the large amount of satellite data, it is not appropriate for a large-scale mapping.

NLSMA approach was applied to extract impervious areas for Amersfoort in the last 30 years using satellite images of 1987, 1992, 1998, 2007 and 2014. A significant increase in impervious surface areas was observed mainly due to the north expansion of urban areas. In the study area we investigated in, the impervious surface increased from **15.87 km^2** to **27.01 km^2** for the last 27 years. Quick urbanization process was observed for the periods from 1987 to 1998 and from 207 to 2014.

The impervious areas maps were used to simulate the runoff in a case of an intensive rainfall event with various reoccurrences. The impervious areas, playing a role as the land cover map, were straightforwardly linked to a rainfall-runoff model. Impervious surfaces of Landsat images acquired on 1987 and 2014 were used to examine the runoff increase with respective to the increasing impervious areas. A statistical description was conducted based on the results of modeling. The inundated area is around **0.29 km^2** for 1987 while it rises to **0.51 km^2** for 2014. A significant increase of **80%** was observed as the result of the expansion of impervious surface areas in these 27 years. However, 30-meter resolution land covers map and DEM are not sufficient to delineate runoff patterns on the street in detail.

Impervious surface map produced by DTC was used to simulate the runoff spatial patterns and risk analysis. Map of impervious areas at a five meter resolution was capable of delineating the extent and spatial patterns of runoff in the urban area. The runoff spatial patterns for the one-hour storm with a return time of half a year, one year, two years and five years are clearly shown in the results section. It can be concluded that the investigated study area can bear a one-hour storm with at least a return time of 2 years.

The rainfall-runoff model is evaluated. The simple model is sufficient to delineate the spatial extent and pattern of runoff responses but overestimation of runoff depth is an important limitation. Possible reasons such as the lack of drainage system, the simplified runoff path are to the most possible causes.

Management recommendations

Great attention should be paid to the regions besides the elevated hills. Location for the Amersfoort central station is a poor chosen location. It is located right beside the only elevated hill, making it being vulnerable for several natural hazards. In addition, the residential area to the north of Amersfoort central station should be concerned with in a case of intensive rainfall with a return time of more than 2 years. Large volumes of runoff were simulated in that region.

On the basis of the runoff patterns, the building risk map in a flood situation can be further mapped when it is associated with a value map of infrastructures and buildings. Risk maps are very valuable in guiding the urban construction department to optimize the urban drainage system, in helping city managers decide whether and where to take actions to protect vulnerable infrastructures when an intensive rainfall is expected.

9. Further research

Further recommended research on the basis of this thesis is described here.

- It is recommended to investigate a more efficient method to minimize the observed underestimation in the built-up areas for Normalized Linear Spectral Mixing Analysis (NLSMA) method.

- As high spatial resolution images are becoming more available, classifications based on object-based image analysis (OBIA) are promising. OBIA utilizes the spectral and contextual information to extract land use and land cover. Therefore, a high accuracy of impervious surface areas mapping by OBIA can be expected. Investigating the impervious surface mapping by OBIA and comparing the results to that of the Decision Tree Classification approach can be a valuable topic to study.

- The rainfall-runoff modeling has some limitations that lead to the unrealistic runoff volumes and depth. Adding the local sewage and drainage system into the model will make the runoff simulation more reliable. In addition, a more advanced runoff modeling can be investigated for a more reliable runoff simulation.

10. References

Amersfoort. (n.d.). In Wikipedia. Retrieved August 21, 2014, from http://en.wikipedia.org/wiki/Amersfoort

Amir Taebi, Ronald L. Droste, (2004). Pollution loads in urban runoff and sanitary wastewater. Science of the total Environment, 327: 175 – 184.

Anderson, J.R., Hardy, E. E., Roach, J. T., and Witmer, R. E. (1976). A land use and land cover classification system for use with remote sense data, U.S. Geol. Survey Prof. Paper 964, 28 pp.

Baltsavias, E. P. (2004). Object Extraction and Revision by Image Analysis Using Existing Geodata and Knowledge: Current Status and Steps towards Operational Systems. ISPRS Journal of Photogrammetry & Remote Sensing 58: 129–51.

Bauer, M. E., Heinert, N. J., Doyle, J. K., & Yuan, F. (2004). Impervious surface mapping and change monitoring using Landsat remote sensing. ASPRS Annual Conference Proceedings, Denver, Colorado, May 2004 (Unpaginated CD ROM).

Bauer, M., Loeffelholz, B., and Wilson, B. (2005). Estimation ,mapping and change analysis of impervious surface area by Landsat remote sensing, Proceedings, Pecora 16 Conference, American Society of Photogrammetry and Remote Sensing, October 23 – 27, 2005, Sioux Falls, South Dakota.

Ben Somers, Gregory P. Asner, Laurent Tits, Pol Coppin, (2011). Endmember variability in Spectral Mixtre Analysis: A review. Remote Sensing of Environment. Volume 115, Issue 7: 1603-1616.

Bo-cai Gao, (1996). NDWI-A normalized difference water index for remote sensing of vegetation liquid water from space. 58(3): 257-266.

Boegh, E., Poulsen, R. N., Butts, M., Abrahamsen, P., Dellwik, E., Hansen, S., et al. (2009). Remote sensing based evapotranspiration and runoff modeling of agricultural, forest and urban flux sites in Denmark: From field to macro-scale. Journal of Hydrology, 377(3 – 4), 300 – 316.

Brabec, E., Schulte, S., & Richards, P. L. (2002). Impervious surface and water quality: A review of current literature and its implications for watershed planning. Journal of Planning Literature, 16, 499 – 514.

Buishand A. & Wijngaard, J., (2007). Statistiek van extreme neerslag voor het stedelijk waterbeheer. T*echnical report TR-295, KNMI, De Bilt*.

Cablk, M.E. and Minor, T.B. (2003). Detecting and discriminating impervious cover with high-resolution IKONOS data using principal component analysis and morphological operators. International

Journal of Remote Sensing, 24, pp. 4627–4645.

Carlson, T. N., & Arthur, S. T. (2000). The impact of land use – land cover changes due to urbanization on surface microclimate and hydrology: A satellite perspective. Global and Planetary Change, 25, 49 – 65.

Civco, D. L.,Hurd, J. D.,Wilson, E. H., Arnold, C. L.,& Prisloe, M. P., Jr. (2002).Quantifying and describing urbanizing landscapes in the northeast United States. Photogrammetric Engineering and Remote Sensing, 68(10), 1083 – 1090.

Cleve, C., M. Kelly, F. R. Kearns, and M. Moritz. (2008). Classification of the Wildland–Urban Interface: A Comparison of Pixel- and Object-Based Classifications Using High-Resolution Aerial Photography. Computers, Environment and Urban Systems 32: 317–26.

Crist, Eric P., Cicone, Rochard C., (1984). A physically-Based Transformation of thematic mapper data—The TM Tasseled Cap. Geoscience and Remote Sensing, Volume: GE-22 Issue: 3: 256 - 263

Elvidge, C., Tuttle, B. T., Sutton, P. C., Baugh, K. E., Howard, A. T., Milesi, C., et al. (2007). Global distribution and density of constructed impervious surfaces. Sensors, 7, 1962 – 1979.

Earth Observation and Science (EROS) Center, (2014). Retrieved from http://eros.usgs.gov/.

Fitzpatrick Gerold, Rosenfield, G. H., (1986). A coefficient of agreement as a measure of thematic classification accuracy. Photogrammetric Enginering & Remote Sensing. 52(2): 223-227.

Gilabert, M. A., Garcia-Haro, F. J., & Melia, J. (2000). A mixture modeling approach to estimate vegetation parameters for heterogeneous canopies in remote sensing. Remote Sensing of Environment, 72, 328–345.

Gillies, R. R., Box, J. B., Symanzik, J., & Rodemaker, E. J. (2003). Effects of urbanization on the aquatic fauna of the Line Creek watershed, Atlanta — A satellite perspective. Remote Sensing of Environment, 86, 411 – 422.

Goetz, S.J., Wright, R.K., Smith, A.J., Zinecker, E. and Schaub, E. (2003) IKONOS imagery for resource management: Tree cover, impervious surfaces and riparian buffer analyses in the mid-Atlantic region. Remote Sensing of Environment, 88, pp.195–208.

Google Earth, (2005). Amersfoort houses and estates, 51°08'39.17"N, 5°23'11.30"W. elevation 2300m. 3D buildings data layer. [Viewed 4 November 2014].

Hugo Priemus, 1998. The randstad and the central Netherlands urban ring: Planners waver between two concepts. European Planning Studies, 6, 443 – 455.

Jensen, J. R., & Cowen, D. C. (1999). Remote sensing of urban/suburban infrastructure and socioeconomic attributes. Photogrammetric Engineering and Remote Sensing, 65, 611 – 622.

Jensen, J. R. (2005). Introductory digital image processing: A remote sensing perspective (Third Edition). Upper Saddle River, NJ: Prentice Hall.

Ji, M., & Jensen, J. R. (1999). Effectiveness of subpixel analysis in detecting and quantifying urban imperviousness from Landsat Thematic Mapper imagery. Geocarto International, 14(4), 31–39.

J. Richard Landis and Gary G. Koch. (1977). The measurement of observer agreement for categorical data. Biometrics, 33(1), 159-174

John C. Davis, (2002). Statistics and Data analysis in Geology(3rd Edition). Printed in the United States of America.

KNMI, (2010). Uurgegevens van het weer in Nederland. Retrieved on June 1, 2010 from: http://www.knmi.nl/klimatologie/uurgegevens/

Landsat Science, 2014. Retrieved from http://landsat.gsfc.nasa.gov/?page_id=9

Lu, D., & Weng, Q. (2004). Spectral mixture analysis of the urban landscape in Indianapolis city with Landsat ETM+ imagery. Photogrammetric Engineering & Remote Sensing, 70(9), 1053– 1062.

Lu, D., & Weng, Q. (2009). Extraction of urban impervious surfaces from IKONOS imagery. International Journal of Remote Sensing, 30(5), 1297 – 1311.

Pal, M., & Mather, P. M., (2003). An assessment of the effectiveness of decision tree methods for land cover classification. Remote Sensing of Environment, 86(4), 554-565.

Phinn, S., Stanford, M., Scarth, P., Murray, A. T., & Shyy, T. (2002). Monitoring the composition and form of urban environments based on the vegetation–impervious surface–soil (VIS) model by sub-pixel analysis techniques. International Journal of Remote Sensing, 23(20), 4131– 4153.

Rashed, T., Weeks, J. R., & Gadalla, M. S. (2001). Revealing the anatomy of cities through spectral mixture analysis of multispectral satellite imagery: a case study of the greater Cairo region, Egypt. Geocarto International, 16(4), 5 –15.

Bing Ruifang, (2004). Principle of Hydrology. China WaterPower Press.

Ridd, M.K., (1995). Exploring a V-I-S (vegetation- impervious surface –soil) model for urban ecosystem analysis through remote sensing: comparative anatomy for cities. International Journal of Remote Sensing, 16(12): 2165-2185.

Russell G. Congalton. (1991). A review of assessing the accuracy of classifications of remotely sensed data. Remote Sensing of Environment, 37, 35-46.

Samuel N. Goward, Brian Markham, Dennis G. Dye, Wayne Dulaney, Jingli Yang, (1991). Normalized difference vegetation index measurements from the advanced very high resolution radiometer. Remote Sensing of Environment. 35 (2-3): 257-277.

Sander Siebelink. (2011). Application of rainfall data from radar versus rain gauge in urban water management. Master thesis, Water Engineering and Management, University of Twente.

Tan, Q., Liu, Z., & Li, X. (2009). Mapping urban surface imperviousness using SPOT multispectral satellite images. Proceedings of IEEE Geoscience and Remote Sensing Symposium (IGARSS 2009), III-346 - III-348, Cape Town. doi:10.1109/IGARSS. 2009.5417773.

Van Der Meer, F., & De Jong, S. M. (2000). Improving the results of spectral unmixing of Landsat Thematic Mapper imagery by enhancing the orthogonality of end-members. International Journal of Remote Sensing, 21, 2781– 2797.

V. Henderson. (2003). The urbanization process and economic growth. Journal of Economic Growth, 8, 47-71, 2003.

Weng, Q. (2008). Remote sensing of Impervious Surfaces: An Overview. In Qihao, W. (Ed.), Remote sensing of impervious surfaces (pp. xvi - xx). CRC Press.

Weng, Q., (2012). Remote sensing of impervious surfaces in the urban areas: Requirements, methods, and trends. Remote Sensing of Environment, 117, 34-49.

Weng, Q., Hu, X., & Lu, D. (2008). Extracting impervious surface from medium spatial resolution multispectral and hyperspectral imagery: A comparison. International Journal of Remote Sensing, 29(11), 3209 – 3232.

Weng, Q., Hu, X., & Liu, H. (2009). Estimating impervious surfaces using linear spectral mixture analysis with multi-temporal ASTER images. International Journal of Remote Sensing, 30(18), 4807 – 4830.

World weather and climate information, 2013. Average weather and climate information. Retrieved from http://www.weather-and-climate.com/average-monthly-Rainfall-Temperature-Sunshine,Utrecht,Netherlands

Wu, C., & Murray, A. T. (2003). Estimating impervious surface distribution by spectral mixture analysis. Remote Sensing of Environment, 84, 493 – 505.

Wu, C., (2004). Normalized spectral mixture analysis for monitoring urban composition using ETM+ imagery. Remote Sensing of Environment, 93, 480 – 492..

Xian, G. and Crain, M., (2005). Assessment of urban growth in Tampa Bay watershed using remote sensing data, Remote Sensing of Environment, 97(@):203 – 215.

Xu, H., (2012) Rule-based impervious surface mapping using high spatial resolution imagery, International Journal of Remote Sensing, 34:1, 27-44.

Yang, L., Huang, C., Homer, C.G., Wylie, B.K., and Coan, M.J.. (2003a). An approach for mapping large-area impervious surfaces: synergistic use of Landsat-7 ETM+ and high spatial resolution imagery, Canadian Journal of Remote Sensing, 29(2): 230-240s

Yang, L., Xian, G., Klaver, J.M., and Deal, B. (2003b). Urban land cover-change detection through sub-pixel imperviousness mapping using remotely sensed data, Photogrammetric Engineering and Remote Sensing, 69(9): 1003-1010.

Yuan, F., and M. E. Bauer. 2006. Mapping Impervious Surface Area Using High Resolution Imagery: A Comparison of Object-Based and Per Pixel Classification. In Proceedings of ASPRS 2006 Annual Conference, Reno, NV, May 1–5.

Zhou, W., & Troy, A. (2008). An object-oriented approach for analyzing and characterizing urban landscape at the parcel level. International Journal of Remote Sensing, 29(11), 3119 ‑ 3135.

Dataset References

IPO Luchtfoto actueel (2011): orthofoto's van heel Nederland in opdracht van het Ministerie van EL&I, mede Ministerie van I&M, de Provinces/IPO, VTS Politie Nederlands, vier waterschappen en twee gemeenten.

AHN-2 (Actueel Hoogtebestand Nederland), (2012). Retrieved from: http://www.ahn.nl/index.html

Esri Nederland, (2014) Kadaster (BAG).

Landsat-5 image, acquired on 5th July, 1987. Retrieved from: http://glovis.usgs.gov.

Landsat-4 image, acquired on 23th May, 1992. Retrieved from: http://glovis.usgs.gov.

Landsat-5 image, acquired on 16th May, 1998. Retrieved from: http://glovis.usgs.gov.

Landsat-7 image, acquired on 15th April, 2007. Retrieved from: http://glovis.usgs.gov.

Landsat-8 image, acquired on 9th March, 2014. Retrieved from: http://glovis.usgs.gov.

FORMOSAT-2 image, acquired on 22nd July, 2013. Retrieved from http://www.geo-airbusds.com/en/160-formosat-2

Appendix

Appendix I 70 random samples used for regression model development

Sample	greenness	Impervious Percent	Sample	greenness	Impervious Percent
1	-0.01	58	*36*	-0.18	92
2	0.30	5	*37*	-0.06	64
3	0.03	34	*38*	-0.26	100
4	0.25	9	*39*	0.14	14
5	0.29	13	*40*	-0.14	90
6	0.01	23	*41*	-0.04	61
7	0.04	66	*42*	-0.26	98
8	0.26	16	*43*	-0.14	79
9	0.25	13	*44*	-0.09	70
10	-0.12	99	*45*	-0.11	69
11	0.27	11	*46*	-0.09	64
12	-0.11	73	*47*	-0.09	92
13	0.34	0	*48*	0.16	14
14	0.19	15	*49*	-0.10	93
15	-0.11	94	*50*	-0.07	53
16	-0.06	83	*51*	-0.20	94
17	-0.13	92	*52*	-0.13	87
18	-0.09	79	*53*	0.06	19
19	0.07	24	*54*	-0.05	43
20	-0.08	78	*55*	0.05	40
21	0.19	10	*56*	0.08	37
22	-0.10	84	*57*	-0.16	85
23	-0.04	67	*58*	0.05	36
24	-0.12	89	*59*	-0.10	91
25	-0.13	97	*60*	-0.25	100
26	-0.01	43	*61*	-0.05	50
27	-0.06	37	*62*	0.08	43
28	0.04	28	*63*	0.09	27
29	0.00	32	*64*	0.18	20
30	-0.18	100	*65*	0.12	14
31	0.00	42	*66*	-0.01	59
32	0.01	29	*67*	0.11	27
33	-0.14	86	*68*	0.11	42
34	-0.02	57	*69*	0.22	1
25	-0.02	53	*70*	0.22	11

Appendix II 110 samples selected for accuracy assessment of regression modeling

Sample Number	Measured impervious surfaces (%)	Estimated Impervious surfaces (%)
1	49	58.72
2	92	76.77
3	95	68.97
4	62	66.52
5	90	85.48
6	100	100
7	81	68.47
8	53	51.11
9	95	100
10	61	55.08
11	51	69.45
12	90	81.47
13	95	82.26
14	65	67.74
15	62	69.70
16	10	34.34
17	64	70.69
18	92	80.94
19	94	89.02
20	85	67.00
21	86	85.48
22	56	51.98
23	61	85.48
24	70	69.95
25	62	65.31
26	90	77.29
27	98	100.00
28	89	88.47
29	96	91.23
30	74	60.81
31	78	68.96
32	73	65.07
33	64	67.25
34	85	71.69
35	100	100.00
36	93	92.91
37	18	49.38
38	87	83.60
39	39	45.16
40	59	63.87
41	69	69.95
42	77	64.35
43	70	80.94
44	52	57.80
45	81	73.20

46	100	91.23
47	63	59.64
48	80	63.87
49	89	80.15
50	48	48.31
51	65	57.35
52	52	62.92
53	87	88.47
54	71	60.57
55	50	51.33
56	61	57.57
57	90	78.33
58	48	46.83
59	58	54.19
60	20	42.91
61	80	70.20
62	66	68.72
63	90	79.37
64	85	72.44
65	57	55.08
66	68	61.74
67	87	85.21
68	94	91.23
69	86	89.02
70	91	86.29
71	84	80.15
72	73	74.72
73	75	69.95
74	89	76.77
75	32	53.75
76	46	62.69
77	66	68.72
78	40	53.97
79	74	74.72
80	48	42.10
81	21	28.90
82	70	69.70
83	93	92.91
84	79	74.98
85	82	68.72
86	71	53.52
87	53	66.52
88	68	63.40
89	76	71.94
90	71	69.70
91	83	80.94
92	99	90.68
93	98	93.19

94	92	90.96
95	34	26.66
96	46	46.20
97	90	94.59
98	85	100.00
99	50	37.18
100	46	44.75
101	11	0.00
102	9	5.25
103	17	13.36
104	11	3.03
105	16	12.81
106	29	21.07
107	9	0.00
108	23	34.34
109	9	0.00
110	24	12.81

Appendix III 110 samples selected for accuracy assessment of Normalized Linear Spectral Mixing Analysis

Sample Number	Measured impervious (%)	Estimated impervious (%)
1	100	100.00
2	67	57.55
3	72	63.49
4	82	69.44
5	42	32.54
6	0	3.65
7	2	0.00
8	56	34.77
9	90	52.09
10	63	56.35
11	25	25.61
12	3	7.43
13	0	0.61
14	2	4.24
15	31	20.45
16	38	32.35
17	26	26.23
18	82	69.72
19	15	18.00
20	100	100.00
21	7	5.42
22	30	36.78
23	72	68.47
24	42	56.75
25	27	23.67
26	79	76.18
27	63	53.83
28	52	49.78
29	54	25.05
30	20	19.81
31	53	45.51
32	69	61.69
33	70	54.97
34	50	19.06
35	30	14.30
36	23	27.07
37	17	25.15
38	20	12.48
39	49	43.49
40	50	37.82
41	24	25.56
42	51	51.58
43	50	54.62
44	100	95.86

45	82	72.18
46	69	68.16
47	100	86.05
48	90	68.48
49	60	45.14
50	46	36.39
51	80	71.66
52	61	56.53
53	55	68.16
54	34	44.76
55	79	83.13
56	46	55.37
57	46	49.84
58	47	54.18
59	44	44.03
60	40	40.91
61	37	40.28
62	67	57.98
63	1	0.00
64	10	8.59
65	9	0.17
66	2	0.59
67	28	34.73
68	15	9.13
69	68	59.20
70	15	33.75
71	23	21.19
72	25	19.79
73	18	14.45
74	33	29.48
75	24	17.02
76	43	36.67
77	75	64.57
78	29	24.95
79	32	22.81
80	30	27.42
81	15	18.67
82	97	87.81
83	6	3.16
84	30	22.29
85	32	26.47
86	30	20.33
87	35	28.33
88	51	42.59
89	29	35.24
90	35	34.51
91	41	34.92
92	36	27.64

93	17	11.28
94	23	29.57
95	38	38.14
96	25	25.29
97	53	48.46
98	27	25.05
99	35	23.58
100	3	0.00
101	37	28.14
102	31	25.55
103	27	23.48
104	58	54.17
105	13	4.88
106	35	26.17
107	36	28.45
108	56	47.82
109	30	28.83
110	38	40.12

Appendix IV NLSMA results of fractions of vegetation IS and soil in years of 1987, 1992, 1998, 2007 and 2014

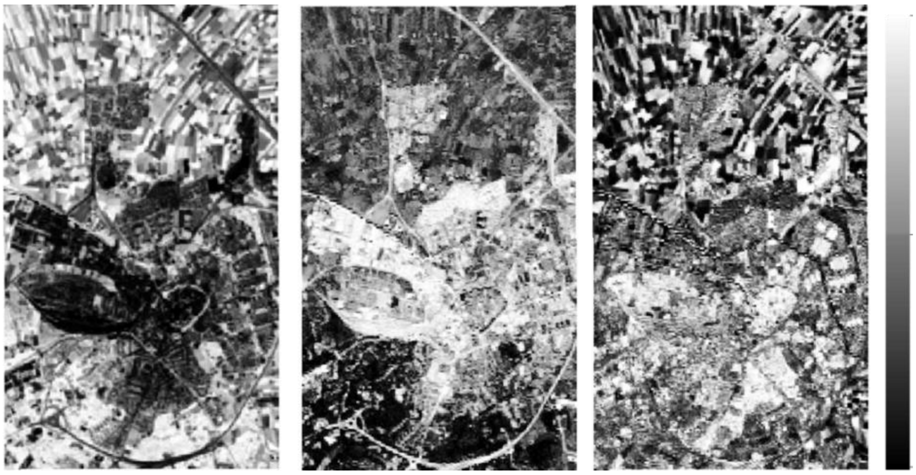

(A)Vegetation (B) Impervious surface (C) Soil

1987

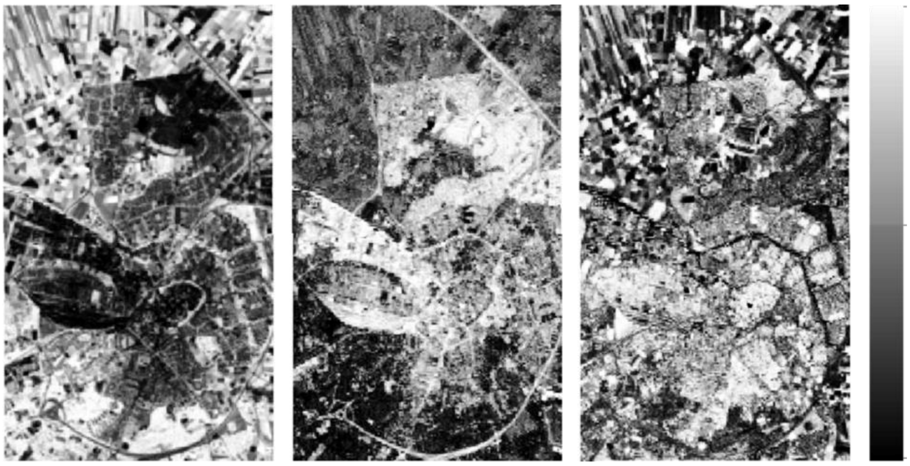

(A)Vegetation (B) Impervious surface (C) Soil

1992

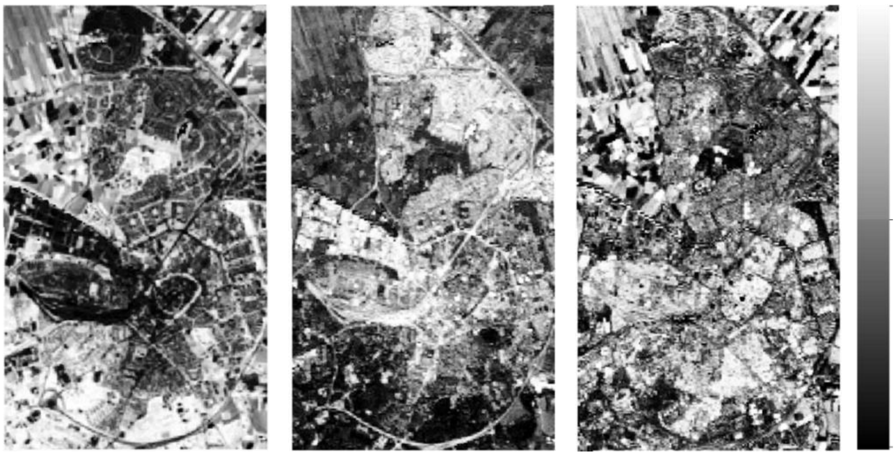

(A)Vegetation (B) Impervious surface (C) Soil

1998

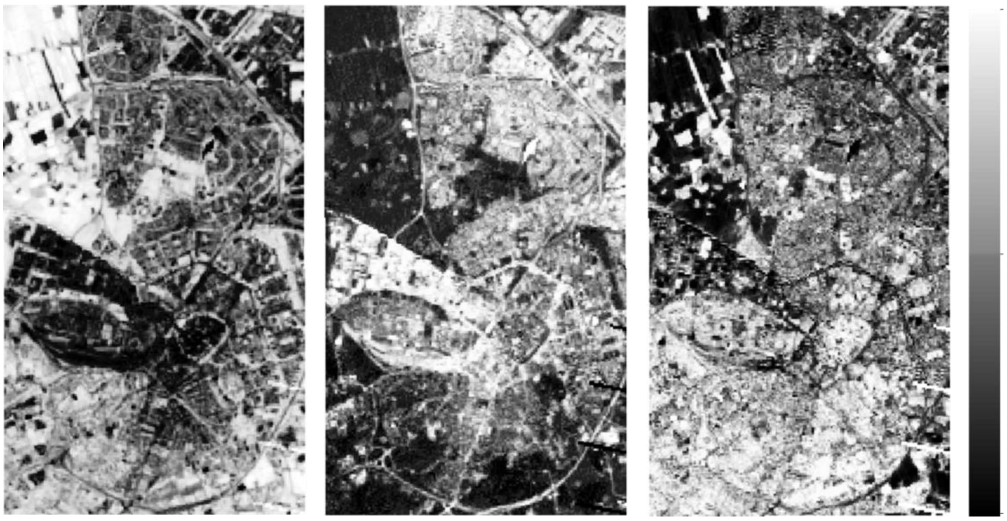

(A)Vegetation (B) Impervious surface (C) Soil

2007

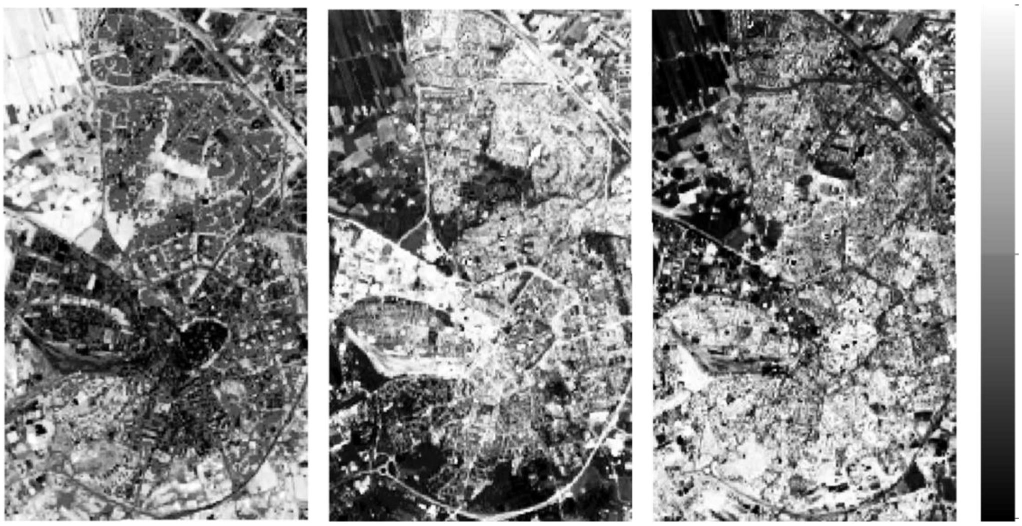

(A)Vegetation (B) Impervious surface (C) Soil

2014

Appendix V Impervious surface mapping by DTC

Appendix VI Extreme rainfall events in the past of Amersfoort

Event Date	Time Start	Duration	Max rainfall amount (mm/h)	Comment
November 25, 2005	12:00	4	25.9	Spatially uniform distribution
July 28, 2006	19:00	1	18.5	Part of very extreme event at the south of Amersfoort
July 5, 2007	2:00	4	30.9	Especially in southern part of Amersfoort
June 3, 2008	0:00	1	21.4	Spatially uniform distribution
Sep. 12, 2008	13:00	1	21.5	Spatially variable in the south-western part of Amersfoort
July 22, 2009	22:30	2	23.0	No comment
August 28, 2009	20:10	2	66.4	No comment
August 4, 2010	15:00	1	85.5	No comment
August 26, 2010	5:00	12	28.0	No comment

Source: Sander Siebelink. (2011). Application of rainfall data from radar versus rain gauge in urban water management. Master thesis, Water Engineering and Management, University of Twent

Appendix VII Model code

```
# model for simulation of runoff
# 3 timesteps of 1 hours

binding
  RainStations=rainstat.map;
  RainTimeSeries=rain.tss;  RainZones=rainzone.map;
  SurfaceWater=rainfall;
  SoilInfiltrationTable=infilcap.tbl;
  LandcoverType=landcover.map;
  InfiltrationCapacity=infilcap.map
  Dem=dem.map;
  Ldd=ldd.map;
  RunOffDTC=runoffDTC;

timer
  1 3 1;

initial
  RainZones=spreadzone(RainStations,0,1);
  InfiltrationCapacity=lookupscalar(SoilInfiltrationTable,LandcoverTy
pe);
  Ldd=lddcreate(Dem,1e31,1e31,1e31,1e31);

dynamic
  SurfaceWater=timeinputscalar(RainTimeSeries,RainZones);
  RunoffPerTimestep,Infiltration=
  accuthresholdflux,
  accuthresholdstate(Ldd,SurfaceWater,InfiltrationCapacity);
  report RunOffDTC=RunoffPerTimestep;
```

Appendix VIII Risk maps of buildings for different intensive rainfalls.

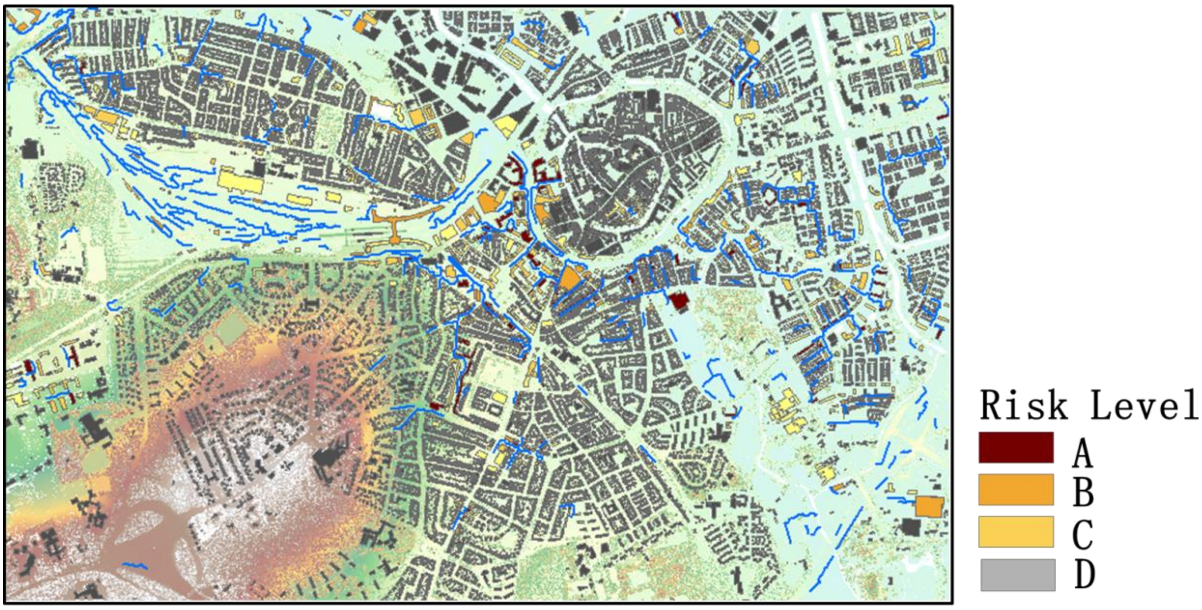

(A) The distribution of risk buildings for a rainfall event of 10 mm/hour

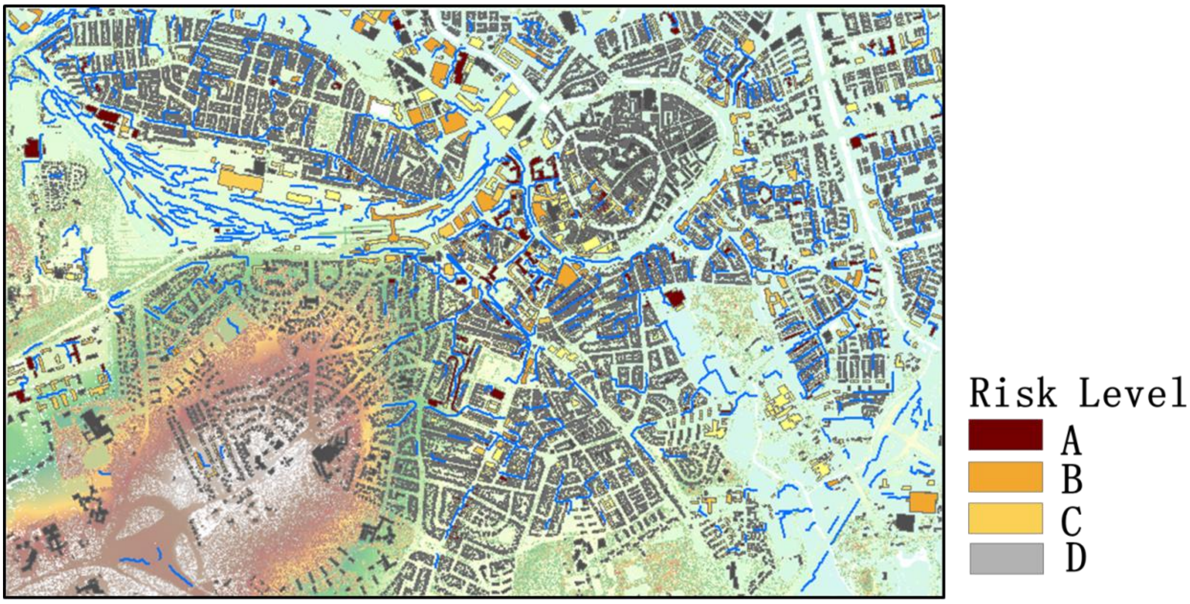

(B) The distribution of risk buildings for a rainfall event of 14 mm/hour.

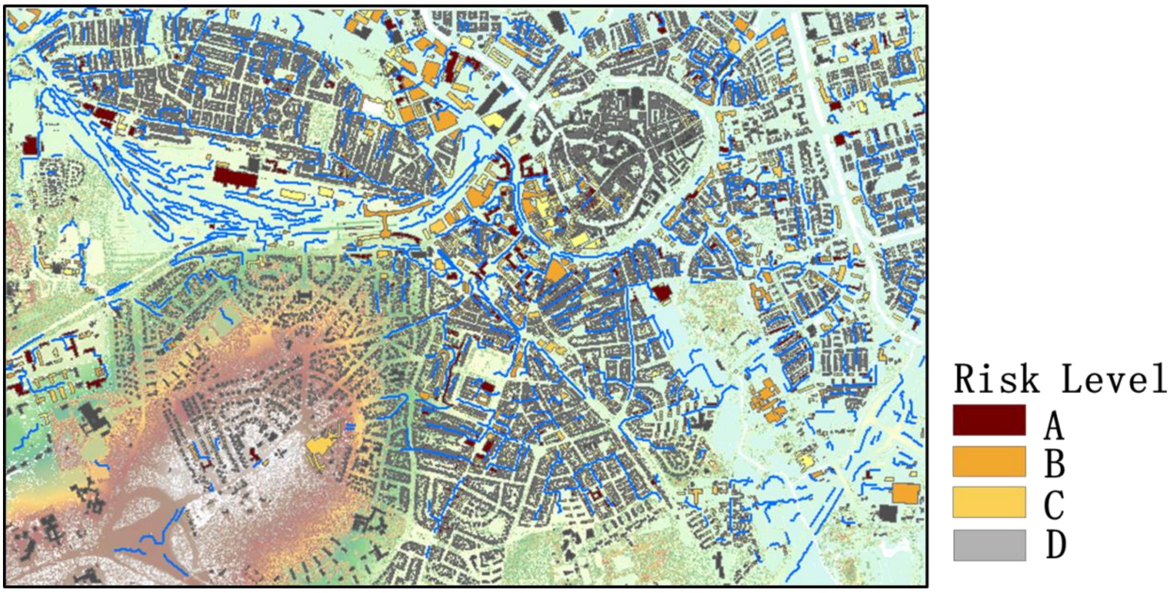

(C) The distribution of risk buildings for a rainfall event of 18 mm/hour.